

Mapping global leaf inclination angle (LIA) based on field measurement data

Sijia Li^{1,2,3}, Hongliang Fang^{1,2}

¹LREIS, Institute of Geographic Sciences and Natural Resources Research, Chinese Academy of Sciences, Beijing 100101, China

²College of Resources and Environment, University of Chinese Academy of Sciences, Beijing 100049, China

³National-Local Joint Engineering Laboratory of Geo-Spatial Information Technology, Hunan University of Science and Technology, Xiangtan 411201, China.

Correspondence to: Sijia Li (lisj.19b@igsrr.ac.cn)

Abstract. Leaf inclination angle (LIA), the angle between leaf surface normal and zenith directions, is a vital trait in radiative transfer, rainfall interception, evapotranspiration, photosynthesis, and hydrological processes. Due to the difficulty in obtaining large-scale field measurement data, LIA is typically assumed to follow the spherical leaf distribution or simply considered constant for different plant types. However, the appropriateness of these simplifications and the global LIA distribution are still unknown. This study compiled global LIA measurements and generated the first global 500 m mean LIA (MLA) product by gap-filling the LIA measurement data using a random forest regressor. Different generation strategies were employed for noncrops and crops. The MLA product was evaluated by validating the nadir leaf projection function ($G(0)$) derived from the MLA product with high-resolution reference data. The global MLA is $41.47^\circ \pm 9.55^\circ$, and the value increases with latitude. The MLAs for different vegetation types follow the order of cereal crops (54.65°) > broadleaf crops (52.35°) > deciduous needleleaf forest (50.05°) > shrubland (49.23°) > evergreen needleleaf forest (47.13°) \approx grassland (47.12°) > deciduous broadleaf forest (41.23°) > evergreen broadleaf forest (34.40°). Cross-validation shows that the predicted MLA presents a medium consistency ($r = 0.75$, $RMSE = 7.15^\circ$) with the validation samples for noncrops, whereas crops show relatively lower correspondence ($r = 0.48$ and 0.60 for broadleaf crops and cereal crops) because of limited LIA measurements and strong seasonality. The global $G(0)$ distribution is opposite to that of the MLA and agrees moderately with the reference data ($r = 0.62$, $RMSE = 0.15$). This study shows that the common spherical and constant LIA assumptions may underestimate the intercept capability for most vegetation. The MLA and $G(0)$ products derived in this study would enhance our knowledge about global LIA and should greatly facilitate remote sensing retrieval and land surface modeling studies.

The global MLA and $G(0)$ products can be accessed at:

Li, S. and Fang, H. 2024, <https://doi.org/10.5281/zenodo.10940673>.

31 1 Introduction

32 Vegetation regulates terrestrial carbon and water cycles through a series of biophysical processes such as photosynthesis,
33 respiration, and transpiration ([Foley et al., 1996](#); [Chen et al., 2019](#)). These biophysical processes are mainly carried by leaves
34 and the characterization of leaves within canopies is vital for remote sensing and earth system modeling ([Ross, 1975](#);
35 [Lawrence et al., 2019](#)). Leaf inclination angle (LIA) denotes the inclination of the leaf or needle to the horizontal plane or the
36 angle between the leaf surface normal and zenith ([Wilson, 1960](#)). LIA is a key canopy structural trait that determines
37 radiative transfer, rainfall interception, evapotranspiration, photosynthesis, and hydrological processes ([Sellers, 1985](#); [Ross,](#)
38 [1981](#); [Mantilla-Perez and Salas Fernandez, 2017](#); [Xiao et al., 2000](#); [Maes and Steppe, 2012](#)). LIA has been used in radiative
39 transfer modeling (RTM), remote sensing inversion, and land surface modeling (LSM) studies ([Tang et al., 2016](#); [Wang and](#)
40 [Fang, 2020](#); [Lawrence et al., 2019](#); [Ross, 1975](#)).

41 At the canopy scale, the probability density of LIA or the fraction of leaf area per unit LIA is expressed as the leaf angle
42 distribution (LAD) ([De Wit, 1965](#)). [De Wit \(1965\)](#) summarized six theoretical LADs, including planophile, erectophile,
43 extremophile, plagiophile, uniform, and spherical distributions. Specifically, the spherical distribution assumes that the
44 relative probability density of the LIA is proportional to the area of the corresponding sphere surface element and its mean
45 leaf inclination angle (MLA) equals 57.3° ($MLA = 57.3^\circ$) ([De Wit, 1965](#)). Furthermore, [Ross \(1981\)](#) defined the inclination
46 index (χ_L) to describe the departure of LAD from the spherical distribution. For the planophile distribution, $\chi_L = 1$; for the
47 erectophile distribution, $\chi_L = -1$; and for the spherical distribution, $\chi_L = 0$. In the radiative transfer regime, LIA is generally
48 represented by the leaf projection function ($G(\theta)$), which is defined as the average projection ratio of unit leaf area in the
49 illumination or viewing direction θ ([Ross, 1981](#); [Nilson, 1971](#)). The spherical distribution is characterized by an isotropic
50 leaf projection function ($G \equiv 0.5$) ([De Wit, 1965](#)).

51 In the field, LIA can be measured directly based on the leaf's geometrical structure or using indirect optical methods ([Lang,](#)
52 [1973](#); [Ryu et al., 2010](#); [Norman and Campbell, 1989](#); [Weiss and Baret, 2017](#)). Using these methods, several LIA
53 measurements have been carried out and some LIA datasets were constructed ([Kattge et al., 2020](#); [Chianucci et al., 2018](#);
54 [Hinojo-Hinojo and Goulden, 2020](#); [Pisek and Adamson, 2020](#)). These field methods are usually time-consuming and labor-
55 intensive and are typically difficult to acquire large-scale LIA ([Li et al., 2023](#)). In addition, the existing LIA datasets have
56 not been comprehensively analyzed. LIA has also been estimated from satellite imagery through empirical relationships or
57 radiative transfer model inversions ([Zou and Möttus, 2015](#); [Bayat et al., 2018](#); [Goel and Thompson, 1984](#)). Remote sensing
58 methods are used primarily for crops in local regions, and the generality of these algorithms is limited ([Li et al., 2023](#)). Due
59 to the difficulty in large-scale LIA measurements and estimations, our knowledge about the global LIA remains lacking.

60 Because our understanding of the global LIA is limited, different LIA simplification strategies have been adopted in various
61 studies. For example, LIA is typically assumed to follow the spherical distribution ([Tang et al., 2016](#); [Zhao et al., 2020](#);
62 [Wang and Fang, 2020](#)). However, this assumption may decrease the accuracy of radiative transfer modeling, significantly
63 underestimate the radiation interception ([Stadt and Lieffers, 2000](#)), and cause large errors (>50%) in leaf area index (LAI)

64 measurements and inversions ([Yan et al., 2021](#)). The spherical LIA assumption may introduce greater error in the nadir
65 direction than other viewing geometries ([Yan et al., 2021](#)), considering the large G variation in this direction ([Wilson, 1959](#)).
66 The lack of global LIA knowledge also limits the retrieval of other vegetation structural parameters([Li et al., 2023](#)). In many
67 LSMs, LIA is commonly treated as a fixed value for different plant function types (PFT) ([Lawrence et al., 2019](#); [Majasalmi](#)
68 [and Bright, 2019](#)). Field LIA measurements have demonstrated that the spherical distribution is not appropriate for forests,
69 and the PFT-dependent LIA ignores LIA variation within the PFT ([Pisek et al., 2013](#); [Yan et al., 2021](#); [Majasalmi and Bright,](#)
70 [2019](#)).

71 This study aims to generate the first global MLA map from existing LIA field measurements using a data-driven gap-filling
72 method. This method involves spatial expansion and upscaling of LIA measurements, and a random forest regressor using
73 input spectral, climate, and PFT data. Based on the global MLA map, we tested whether the spherical LIA assumption is
74 appropriate at the global scale. The new MLA map was validated by comparing the nadir G ($G(0)$) derived from the MLA
75 with high-resolution reference data. Section 2 outlines the materials and methods employed to generate and evaluate the
76 global MLA. Section 3 presents the global LIA measurements, global MLA and $G(0)$, and evaluation results. Section 4
77 discusses the performance of the global MLA and $G(0)$, the usage of the new MLA map, and the limitations of the study.
78 Section 5 presents the main conclusions.

79 **2 Materials and methods**

80 **2.1 LIA measurement data**

81 **2.1.1 TRY LIA dataset**

82 TRY is a network of vegetation scientists headed by Future Earth, the Max Planck Institute for Biogeochemistry, and
83 German Centre for Integrative Biodiversity Research, providing a global database of curated plant traits (the TRY database)
84 (<https://www.trydb.org/TryWeb/Home.php>). Since its establishment in 2007, the TRY database has continuously evolved
85 and has become one of the most widely used vegetation trait databases. The latest V6 version (released on October 13, 2022)
86 employed in this study contains 15,409,681 trait records covering 305,594 plant taxa ([Kattge et al., 2020](#)). In this database,
87 LIA was recorded as a numerical or categorical variable. After data extraction and checking, 31,043 valid records were used,
88 which include numerical LIA, locations, and species. Many measurements lack location information, whereas, for some
89 locations, there are many measurements for individual species. The spatial distribution map appears relatively sparse despite
90 a large volume of data (Fig. 1). The LIA measurements in South America are mainly from palms.

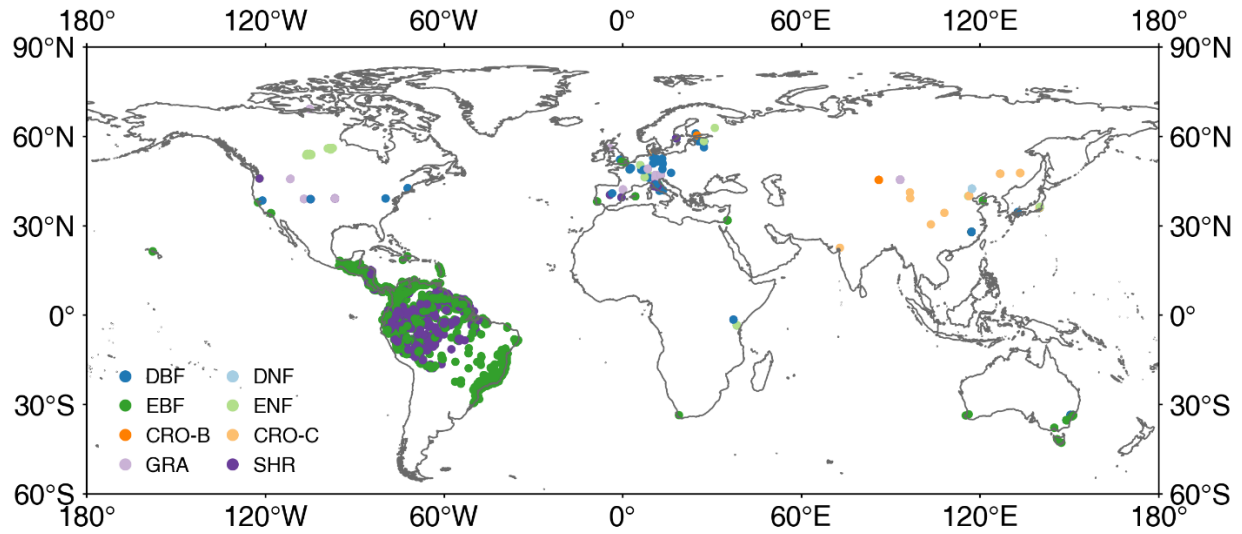


Figure 1. The locations of global leaf inclination angle measurements. DBF: deciduous broadleaf forest, DNF: deciduous needleleaf forest, EBF: evergreen broadleaf forest, ENF: evergreen needleleaf forest, CRO-B: broadleaf crops, CRO-C: cereal crops, GRA: grassland, SHR: shrubland.

2.1.2 LIA data from the literature

The LIA measurements in published literature were collected via keyword search (leaf angle, leaf inclination angle, and leaf tilt angle) in the Web of Science, Google Scholar, Google, and Chinese documentary databases. The LIA, location, and species information were manually extracted from the literature (Fig. 1). Several LIA measurements were already included in the TRY database (Chianucci et al., 2018; Pisek and Adamson, 2020). After aggregating LIA measurements for the same species at the same location, 780 LIA records were accessed from previous studies (Hinojo-Hinojo and Goulden, 2020; Pisek et al., 2022; Chen et al., 2021).

2.1.3 Manual LIA extraction

Only a few measurements in the northern tundra region were obtained, and the measurements in tropical regions are dominated by palm trees (Fig. 1). Therefore, LIA data for the northern tundra and tropical regions were extracted from horizontal side-view photographs searched from Google (Fig. S1).

ImageJ software (<https://imagej.nih.gov/ij/>) was used to process the leveled photographs and derive LIA following the method of Pisek et al. (2011). The TRY species location data (848,919, Fig. S3b) (Jan 03, 2022) were used to obtain the dominant species information in tropical rainforests and the northern tundra. The species location points in these two vegetation types were spatially filtered and the frequency of occurrence for each species was counted. The species with a high frequency of occurrence were selected to measure the LIA. For each species, more than 75 leaves perpendicular to the

viewing direction were selected and processed based on visual judgment to ensure the stability and reliability of the MLA (Pisek et al., 2013). In total, the MLA of 104 species was manually derived. In this study, most LIA measurements are obtained with protractor and level digital photogrammetry, especially for needleleaf species. Therefore, the distinction between branches and leaves is considered. The diverse LIA records from different sources were sorted to match the TRY species and to get the PFT based on the TRY Categorical Traits Dataset 2018 (<https://www.try-db.org/TryWeb/Data.php#3>). The MLA was calculated for the LIA records with different forms. If there were multiple LIA records for the same species, the mean value was computed for the same location and species. In total, 5,554 LIA records of 1,194 species were collected, covering the growing season from 2001 to 2022. LIA location replicates per species range from 1 to 330, and most replicates (98 %) are less than 50. Considering the different numbers of records for each species, the LIA data was further aggregated by species.

2.2 Remote sensing data

2.2.1 Ancillary data used for MLA mapping

The ancillary data used for global MLA mapping and analysis are listed in Table 1. The PFT classification system in the MODIS global 500 m land cover type product (MCD12Q1.061) was used and mode-aggregated from 2001 to 2022 to match the LIA measurements (Fig. S2) (Sulla-Menashe et al., 2019). The 2001–2022 Landsat surface reflectance (Level 2, Collection 2, Tier 1) (Crawford et al., 2023), including Landsat 5 (2001–2012), Landsat 7 (2012–2013), and Landsat 8 (2013–2022) was utilized to generate a global 30 m PFT map (Section 2.3.1), which was subsequently employed for LIA upscaling. The 2001–2022 MODIS bidirectional reflectance distribution function (BRDF) model parameters dataset (MCD43A1 C6.1) (Schaaf and Wang, 2015b) and nadir BRDF adjusted reflectance dataset (MCD43A4 V6 NBAR) (Schaaf and Wang, 2015a) are produced daily using 16 days of Terra and Aqua MODIS data at 500 m resolution and were utilized as predictive variables. Due to the scarcity of crop LIAs and the lack of location information for existing crop LIA measurements, fine-resolution (10/30 m) crop-type maps (Table 1) in 2018 were employed to support crop LIA mapping. Other data include the ERA5-Land reanalysis data, the ALOS digital elevation model (AW3D30 V3.2), and the 2001–2022 MODIS LAI product (MCD15A2H) (Myneni, 2015). The LAI product was averaged and aggregated from 2001–2022. Most earth observation data were accessed and processed in Google Earth Engine (GEE) (<https://earthengine.google.com/>).

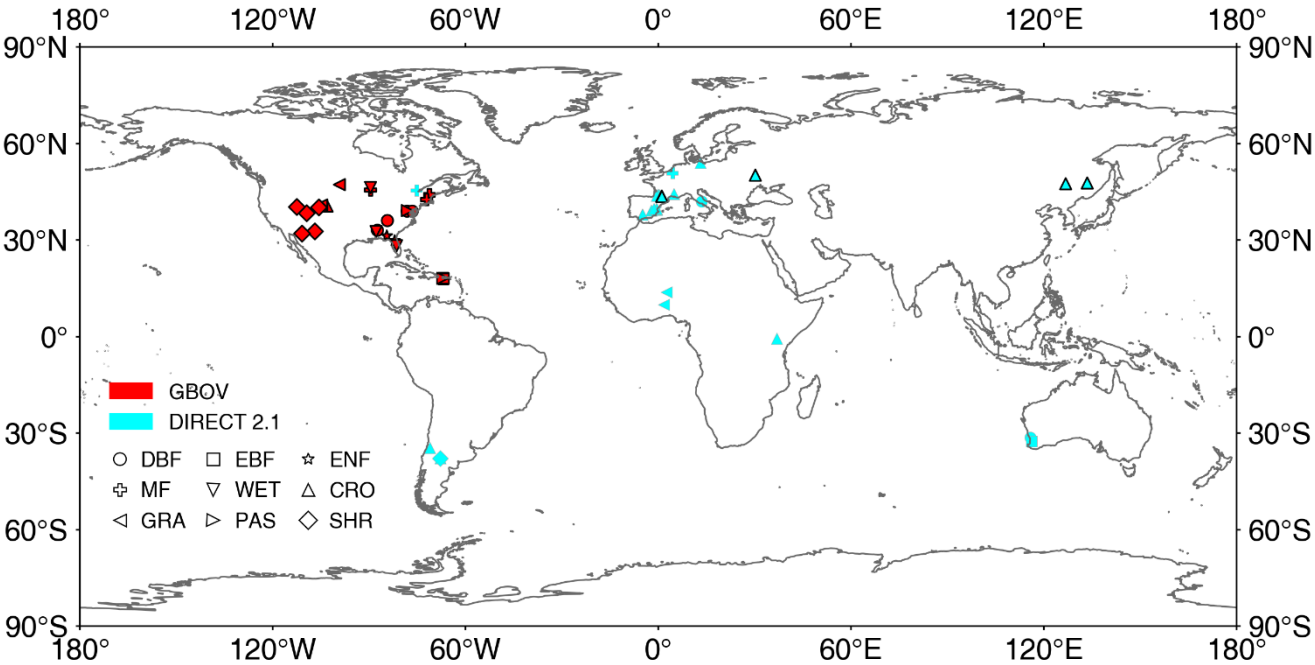
Table 1. Remote sensing data for global MLA mapping. BRDF: bidirectional reflectance distribution function.

Category	Data	Year	Spatial resolution	Temporal resolution	Reference
Plant function type	MCD12Q1 C6	2001–2022	500 m	Yearly	(Sulla-Menashe et al., 2019)
Surface reflectance	Landsat collection 2	2001–2022	30 m	16 days	(Crawford et al., 2023)
	MCD43A4 V6 NBAR	2001–2022	500 m	Daily	(Schaaf and Wang, 2015a)
BRDF	MCD43A1 C6.1	2001–2022	500 m	Daily	(Schaaf and Wang, 2015b)
Crop type	Cropland Data Layers (CDL)	2018	30 m	Yearly	(Boryan et al., 2011)

	EUCROPMAP		2018	10 m	Yearly	(D'andrimont et al., 2021)
	AAFC Annual Crop Inventory		2018	30 m	Yearly	(Fisette et al., 2013)
	Northeast China crop-type map		2018	30 m	Yearly	(You et al., 2021)
	NESEA-Rice10		2018	10 m	Yearly	(Han et al., 2021)
	China maize map		2018	30 m	Yearly	(Shen et al., 2022)
	China winter wheat map		2018	30 m	Yearly	(Dong et al., 2020)
Climate	ERA5-Land		2001–2022	0.1°	Monthly	(Muñoz-Sabater et al., 2021)
Terrain	AW3D30 V3.2		—	30 m	—	(Tadono et al., 2014)

138
2.2.2 High-resolution reference data

139
The high-resolution reference datasets provided by Ground Based Observations for Validation (GBOV,
140
<https://land.copernicus.eu/global/gbov/dataaccessLP/>) and DIRECT 2.1 (<https://calvalportal.ceos.org/lpv-direct-v2.1>) were
141
used to evaluate the generated global MLA (Fig. 2). These datasets provide high-resolution (20/30 m) LAI, effective LAI
142
(LAIe), and fractional vegetation cover (FVC) data over a 3 km × 3 km area centered on each site generated using empirical
143
relationships between various vegetation indices and ground measurements ([Li et al., 2022](#); [Brown et al., 2020](#)). GBOV has
144
provided continuous high-resolution reference data since 2013 (Fig. 2).



145
146
Figure 2. Locations of GBOV and DIRECT 2.1 sites used in this study. CRO: Cultivated crops, MF: Mixed forest, PAS: Pasture/hay,
147
WET: Woody wetlands. See Fig. 1 for other acronyms. The black frame indicates those sites with >5 continuous records.

148 2.3 Mapping global LIA

149 2.3.1 Data preparation

150 Many studies have treated LIA as a species-specific static trait and ignored within-species variations when LIA
151 measurements are limited ([Pisek et al., 2022](#); [Toda et al., 2022](#); [Raabe et al., 2015](#)). Following the rationale, the spatial
152 coverage of LIA measurements was expanded, and those records without location information were utilized (section 2.1.1).
153 Under this assumption, the LIA measurements were expanded through TRY species location data with species name
154 matching. When a species had multiple LIA observations at different locations, the nearest LIA was assigned to the TRY
155 species location. Visual inspections were conducted to remove potential TRY location biases, especially for non-vegetated
156 points such as water bodies and deserts. After spatial expansion, the number of LIAs reached 12,328 (Fig. S3c).
157 In this study, the scale gap between field measurements and satellite remote sensing data was fully considered. To upscale
158 the LIA measurements to the satellite resolution (500 m), a 30 m PFT map was first derived from Landsat reflectance using a
159 random forest classification method. The random forest was trained at a 500 m scale using the mode-aggregated MODIS
160 PFT classification map as training samples to generate a 30 m PFT map by hierarchically selecting homogeneous pixels
161 (with a coefficient of variation in reflectance < 0.2). The classification features were the same as those in the MODIS
162 classification algorithm ([Sulla-Menashe et al., 2019](#)). For a 500 m pixel with multiple PFTs (Fig. 3a), when one PFT had no
163 LIA measurement, the LIA of the PFT was assigned with the value of its nearest neighbor within 100 km with the same PFT.
164 In field measurement, the entire canopy LIA is calculated as the average of all measured leaf LIAs weighted by leaf area
165 ([Zou et al., 2014](#); [De Wit, 1965](#); [Yan et al., 2021](#)). Leaves with larger areas have higher weights. Upscaling LIA from 30 m
166 to 500 m follows the same rationale as that from leaf to canopy scale. For a 30 m pixel with a higher LAI, the weight of the
167 pixel is higher. Therefore, The 500 m MLA was computed as the weighted average of the enhanced vegetation index (EVI2)
168 considering a linear relationship between LAI and EVI2 ([Dong et al., 2019](#); [Alexandridis et al., 2019](#)).

$$169 \quad MLA_{500m} = \frac{\sum MLA_{30m} \times EVI2_{30m}}{\sum EVI2_{30m}} \quad (1)$$

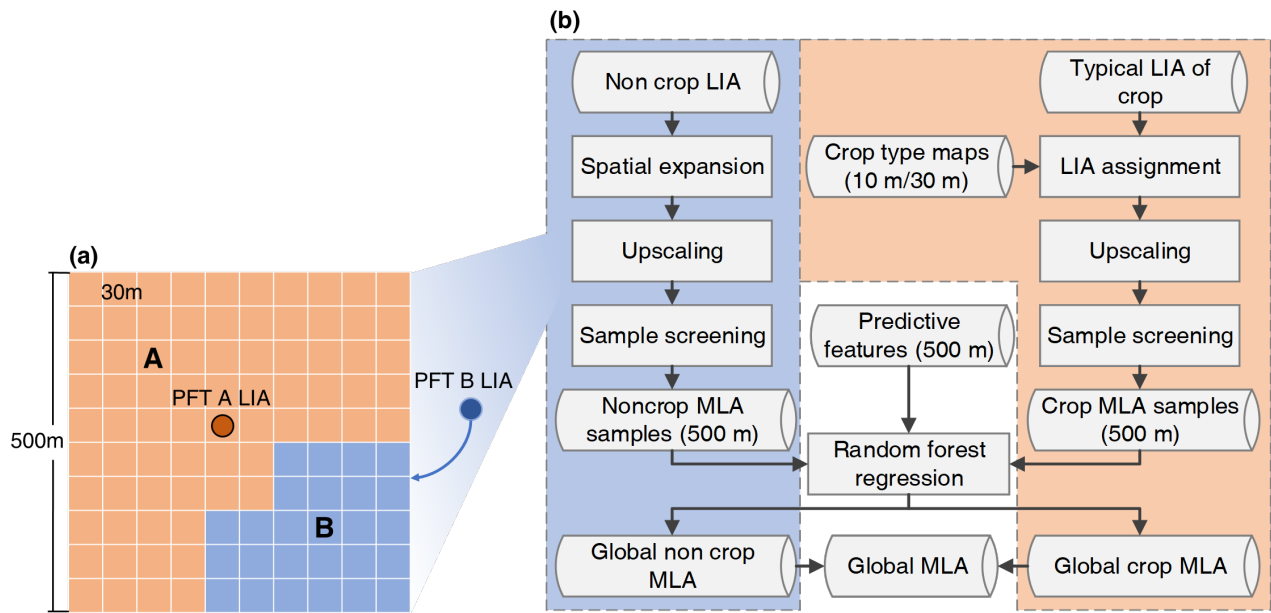


Figure 3. Leaf inclination angle (LIA) upscaling (a) and global mean LIA (MLA) mapping (b) strategies.

The 500 m upscaled MLA samples were further refined to select the most representative samples following three criteria: 1) the coefficient of variation of the 30 m EVI2 in the 500 m pixel is less than 0.2, 2) the vegetation proportion in the 500 m pixel is greater than 0.8, and 3) the proportion of PFTs represented by the MLA measurements in the 500 m pixel is greater than 0.4. The final number of samples after refinement is 3,013 (Fig. 4).

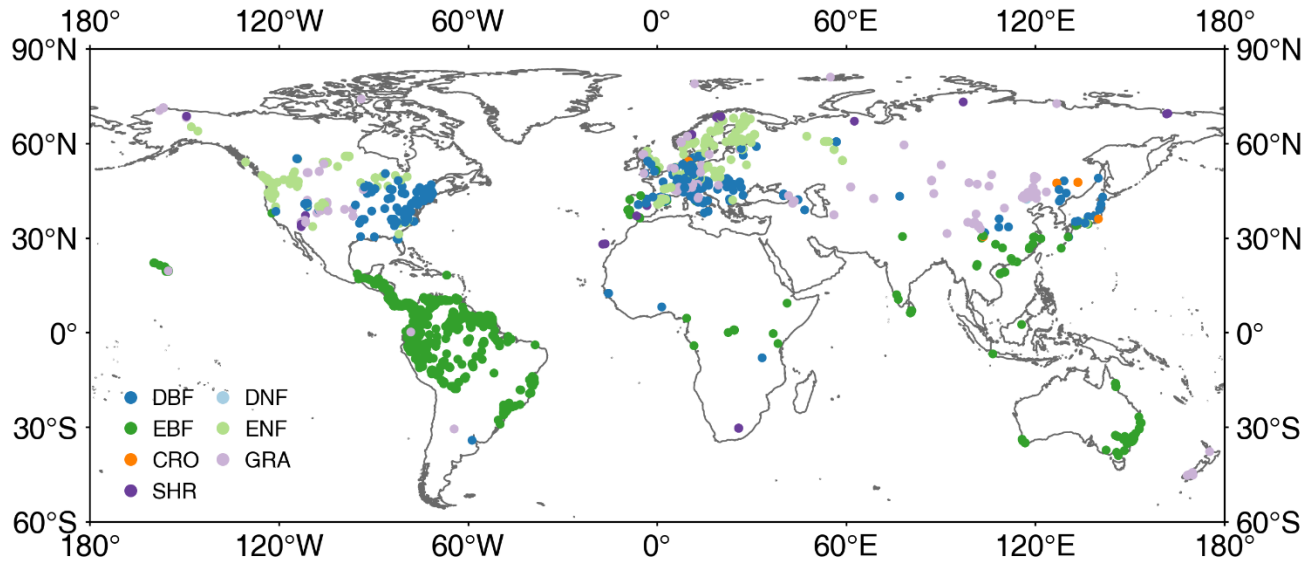


Figure 4. Distribution of global mean leaf inclination angle samples after screening. See Fig. 1 for acronyms.

178 **2.3.2 Global MLA mapping**

179 Different mapping strategies were employed for noncrops and crops (Fig. 3b) considering the small number of valid crop
180 samples (Fig. 4) and the lack of location information for most crop samples. For noncrops, the upscaled 500 m MLA
181 samples were used to train a random forest regressor to predict the global MLA from different features (Table 2). To reduce
182 computational complexity and potential overfitting, a feature selection process was conducted based on the variable
183 importance (the sum of the decrease in Gini impurity index over all trees in the forest) computed by the model, and only the
184 40 most important variables were used in the final prediction. During the training process, the out-of-bag error was
185 minimized to obtain the optimal hyperparameters. The prediction performance of the random forest regressor was evaluated
186 using a ten-fold cross-validation approach with upscaled MLA samples.

187 For crops, the measured MLA values were averaged for different crop types as a typical MLA (Table S2). After assigning
188 typical MLAs for different crops with high-resolution crop maps (Table 1), the high-resolution crop MLA were upscaled to
189 500 m as training samples (Eq. (1)). Only the samples with a crop area ratio > 80% within a 500 m pixel were selected for
190 training. The crops were further divided into broadleaf crops and cereal crops and processed with the same procedure used
191 for noncrops (Fig. 3b). All procedures were conducted on GEE under the WGS-84 geographic coordinate system.

192

193 **Table 2.** Predictive features in global MLA mapping.

Category	Features	Variables	Number
Spectral	Blue, green, red, near-infrared reflectance	10%, 33%, 50%, 67%, 90% quantiles and standard deviation	24
	NDVI	10%, 33%, 50%, 67%, 90% quantiles and standard deviation	6
BRDF	Kernel coefficients of the red band	10%, 33%, 50%, 67%, 90% quantiles and standard deviation	18
	Kernel coefficients of near-infrared band	10%, 33%, 50%, 67%, 90% quantiles and standard deviation	18
PFT	PFT	Constant	1
Climate	Solar downward radiation	Mean and standard deviation	2
	Temperature	Mean and standard deviation	2
	Precipitation	Mean and standard deviation	2
Terrain	Elevation	Constant	1
	Slope	Constant	1
	Aspect	Constant	1

194 **2.4 Evaluation of global MLA**

195 The global MLA map was indirectly evaluated using the nadir leaf projection function, because of the lack of high-resolution
196 reference MLA. G(0) is important because it is coherent with the satellite nadir observations. The global G(0) was derived
197 from the MLA and evaluated with high-resolution reference following the upscaling scheme recommended by the Land
198 Product Validation (LPV) Subgroup of the Committee on Earth Observation Satellites (CEOS) (<http://lpvs.gsfc.nasa.gov/>).

199 Assuming a single-parameter ellipsoidal leaf angle distribution ([Campbell, 1990](#); [Wang et al., 2007](#)), the parameter χ , the
 200 ratio of the horizontal and vertical axes of an ellipsoid, was first derived from MLA in radians. Compared to other models,
 201 the single-parameter ellipsoidal leaf angle distribution is a relatively more accurate and simpler model and has been used in
 202 many remote sensing studies ([Campbell, 1990](#); [Wang et al., 2007](#); [Kuusk, 2001](#); [Verhoef et al., 2007](#)).

$$203 \quad \chi = -3 + \left(\frac{MLA}{9.65}\right)^{-0.6061} \quad (2)$$

204 The $G(\theta)$ value in the nadir direction ($\theta=0^\circ$) was calculated using the following analytical formula.

$$205 \quad G(\theta) = \frac{\sqrt{(\chi^2 + \tan^2 \theta) \cos \theta}}{\chi + 1.774(\chi + 1.182)^{-0.73}} \quad (3)$$

206 The reference $G(0)$ was derived from high-resolution LAI, FVC, and clumping index (CI) ($=LAI_e/LAI$) with the Beer-
 207 Lambert law (Fig. S4) ([Nilson, 1971](#)).

$$208 \quad P(\theta) = \exp^{-\frac{G(\theta)*LAI*CI(\theta)}{\cos(\theta)}} \quad (4)$$

209 Where $P(\theta)$, $CI(\theta)$, and $G(\theta)$ denote the gap fraction, CI, and G in direction θ , respectively. Specifically, the gap fraction in
 210 the nadir direction can be expressed by FVC.

$$211 \quad P(0) = 1 - FVC \quad (5)$$

212 Therefore, the reference $G(0)$ was derived using the following formula.

$$213 \quad G(0)_CI(0) = -\frac{\ln(1-FVC)}{CI(0)*LAI} \quad (6)$$

214 By using the whole CI as the nadir CI ($CI(0)$) in the above equation ([Fang et al., 2021](#); [Li et al., 2022](#)), $G(0)$ was calculated
 215 as follows:

$$216 \quad G(0)_CI \approx -\frac{\ln(1-FVC)}{CI*LAI} \quad (7)$$

217 The MLA product was first upscaled to 3 km through a weighted averaging method using the MODIS LAI to derive $G(0)$
 218 (Eq. (3)). The reference LAI, FVC, and CI were also upscaled to 3 km through simple averaging to compute the reference
 219 $G(0)$ (Eq. (7)). The MLA-derived $G(0)$ and the reference $G(0)$ were compared at the $3 \text{ km} \times 3 \text{ km}$ area around each site. The
 220 correlation coefficient (r), bias, and root mean square error (RMSE) were calculated as the evaluation metrics, as follows:

$$221 \quad r = \sqrt{1 - \frac{\sum_{i=1}^n (\hat{y}_i - y_i)^2}{\sum_{i=1}^n (y_i - \bar{y})^2}} \quad (8)$$

$$222 \quad Bias = \frac{1}{n} \sum_{i=1}^n (\hat{y} - y_i) \quad (9)$$

223

$$RMSE = \sqrt{\frac{1}{n} \sum_{i=1}^n (\hat{y} - y_i)^2}$$

224

(10)

224

where \hat{y}_i , y_i , and n denote the MLA-derived $G(0)$, reference $G(0)$, and the number of $G(0)$, respectively.

225

3 Results

226

3.1 Global measured LIA values

227

The species-aggregated LIA was employed in the analysis of global LIA measurements. Fig. 5 shows the distributions of

228

global measured LIA values for different PFTs. The global measured MLA is 40.74° and generally follows the order of

229

CRO-C > GRA > ENF > CRO-B > EBF > SHR > DNF > DBF (Table 3). Cereal crops exhibit the highest MLA (59.11°),

230

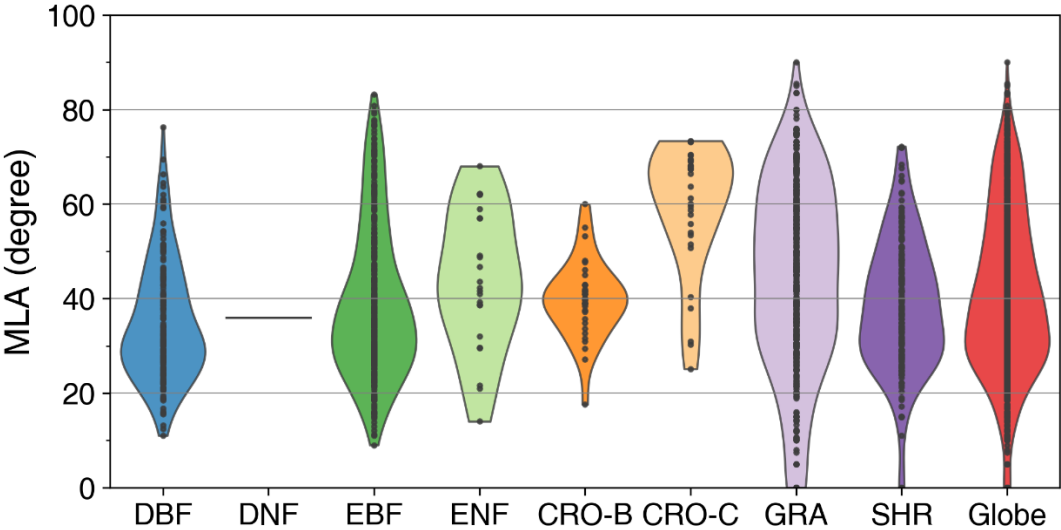
whereas DBF has the most horizontal leaves (MLA = 34.94°). GRA and EBF show large LIA variations (Std = 20.44° and

231

17.17°), whereas CRO-B exhibits a small range. The DNF LIA measurements are only for one species and show very little

232

variation (Fig. 5).



233

234

235

Figure 5. Distribution of global mean LIA (MLA) for different plant function types (see Fig. 1 for acronyms). The last shape shows the global average. Statistics are conducted for each species as represented by points in the figure.

236

237

238

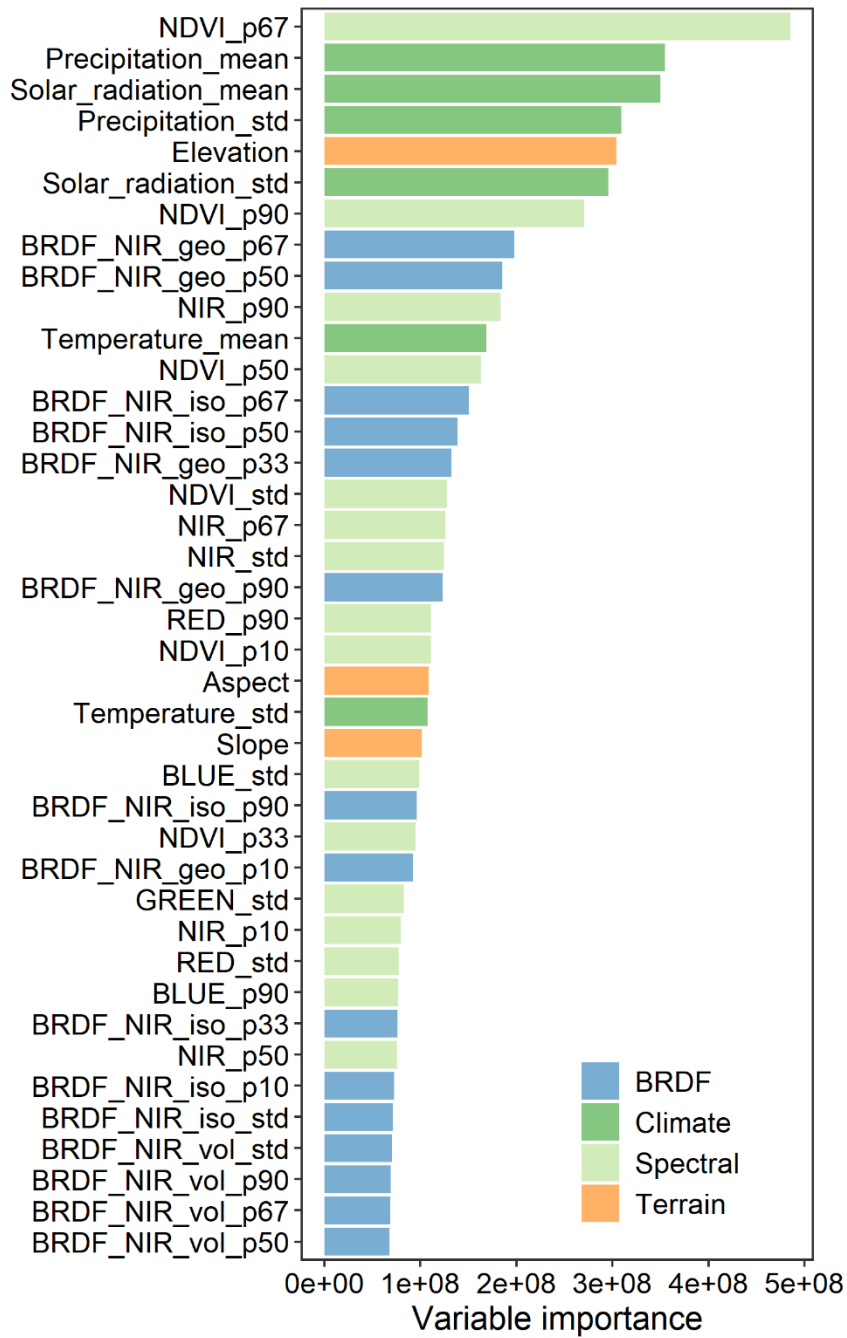
Table 3. Statistics of leaf inclination angle measured for different plant functional types (PFT). STD is the standard deviation. The inclination index (χ_L) is converted from mean leaf inclination angle (MLA) ($\chi_L = 2\cos(\text{MLA}) - 1$) ([Lawrence et al., 2019](#)).

PFT	DBF	DNF	EBF	ENF	CRO-B	CRO-C	GRA	SHR	Globe
Number of species	171	1	347	23	32	31	399	190	1194
Mean(°)	34.94	35.88	39.30	43.69	39.71	59.11	44.13	38.32	40.74

STD (°)	12.40	0.00	16.11	14.40	8.11	13.28	20.17	13.80	17.12
χ_L	0.64	0.62	0.55	0.45	0.54	0.03	0.44	0.57	0.52

239 **3.2 The relationships between MLA and other variables**

240 Fig. 6 shows the importance of the top 40 variables in the MLA prediction obtained from the random forest regression model.
241 The importance of these 40 variables accounts for 78% of the total importance among all 76 variables. Spectral features
242 account for 30% of the importance, which is higher than that of other features. Among the spectral features, NDVI, near-
243 infrared (NIR) band, and red band reflectance are most critical for MLA prediction. The importance of BRDF features is
244 comparable to that of climatic variables (21% vs. 20%), followed by terrain features (7%). Among the BRDF features, the
245 NIR BRDF information shows a higher contribution than the red band, with importance in the following order: geometrically
246 scattered kernel> isotropic scattering kernel > volumetric scattering kernel. The importance ranking of the climatic variables
247 follows the order of precipitation \approx solar radiation > temperature. In addition, elevation, slope, and aspect significantly
248 impact on the MLA prediction.



249

250 **Figure 6.** The importance of variables in the mean leaf inclination angle prediction. NIR, Red, Green, and Blue denote the nadir
 251 reflectance in near-infrared, red, green, and blue bands, respectively; geo, iso, and vol represent kernel coefficients of geometric-optical
 252 surface scattering, isotropic scattering, and volumetric scattering, respectively. The suffixes p××, mean, and std represent ××% quantile,
 253 mean, and standard deviation, respectively.

Fig. 7 illustrates the relationships between the upscaled MLA samples and the 16 most important variables. Overall, MLA decreases with the increase of NDVI, NIR reflectance, and NIR BRDF kernel parameters, whereas it increases with the standard deviation of NDVI. MLA is negatively correlated with solar radiation, precipitation, and temperature. Additionally, MLA increases with increasing the standard deviation of solar radiation (corresponding to mid-to-high latitude regions), while it decreases with the increase in the standard deviation of precipitation (corresponding to tropical and subtropical regions with high precipitation). MLA increases slightly with altitude and then decreases.

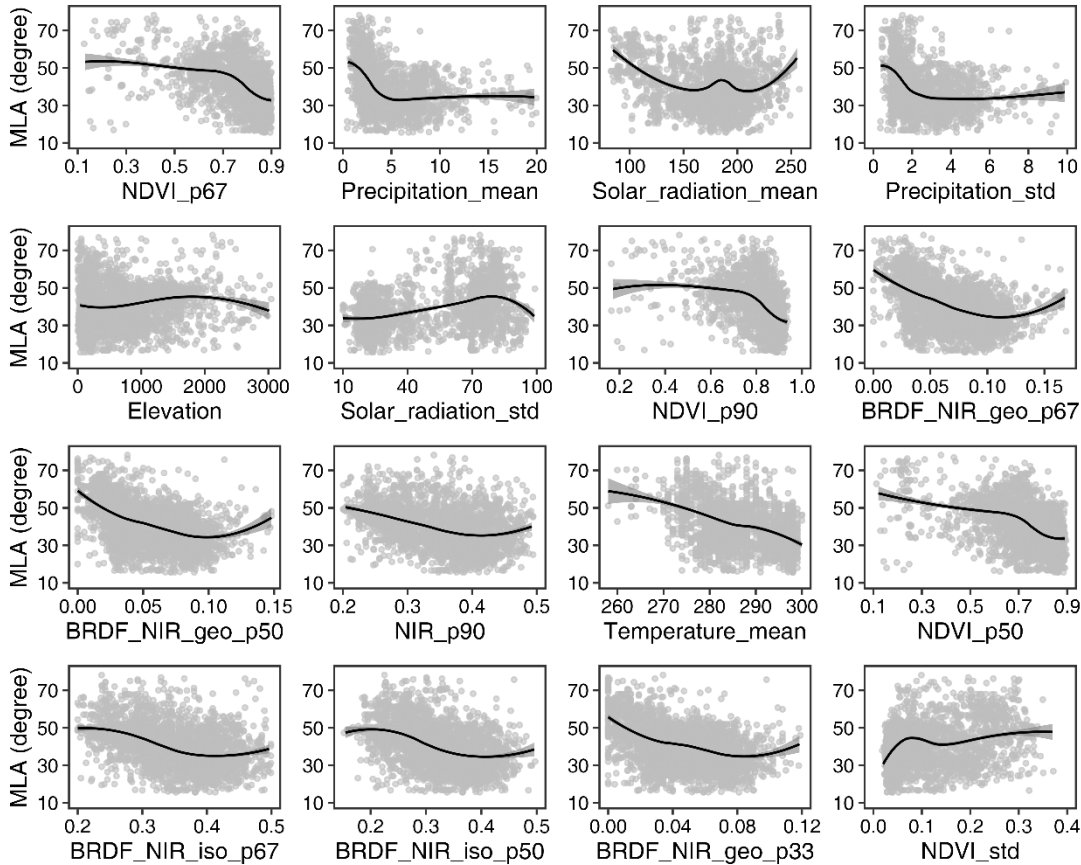
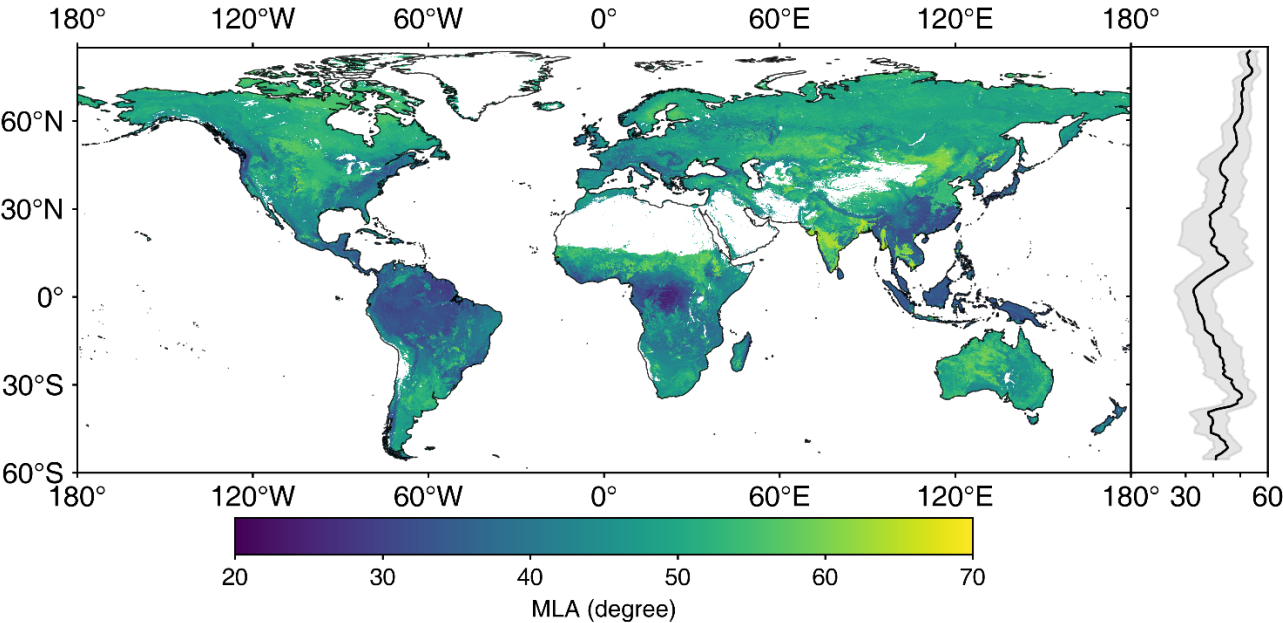


Figure 7. Relationships between mean leaf inclination angle (MLA) and different predictive variables. See Fig. 6 for different variables.

3.3 Global MLA and G(0) maps

Fig. 8 shows the spatial distribution of the global 500 m MLA product. Central Asia (grasslands), southern India (cereal crops), and the central United States (grasslands and cereal crops) show higher MLAs of approximately 60°, whereas the rainforests and Southeast Asia forests have more horizontal leaves with MLAs of around 30° (Fig. 8 and S2). MLA increases with latitude, from $32.93 \pm 7.03^\circ$ around the equator ($\sim 1.5^\circ$ N) to $53.48 \pm 3.20^\circ$ in the northern tundra ($\sim 76.5^\circ$ N). Variation in MLA decreases as latitude increases (Fig. 8). Among different PFTs, cereal crops show the highest MLA ($54.65 \pm 6.28^\circ$),

268 while evergreen broadleaf forest has the lowest MLA ($34.40 \pm 6.42^\circ$), and PFTs follow the order: CRO-C > CRO-B > DNF >
 269 SHR > ENF \approx GRA > DBF > EBF (Table 4). Grassland, broadleaf forest, and evergreen needleleaf forests show larger MLA
 270 variations than other PFTs, whereas deciduous needleleaf forests show minimal variation. The global vegetation MLA is
 271 41.47° , with a standard deviation of 9.55° , which is comparable to the MLA of DBF ($41.23 \pm 6.58^\circ$) (Fig. 9a and Table 4).

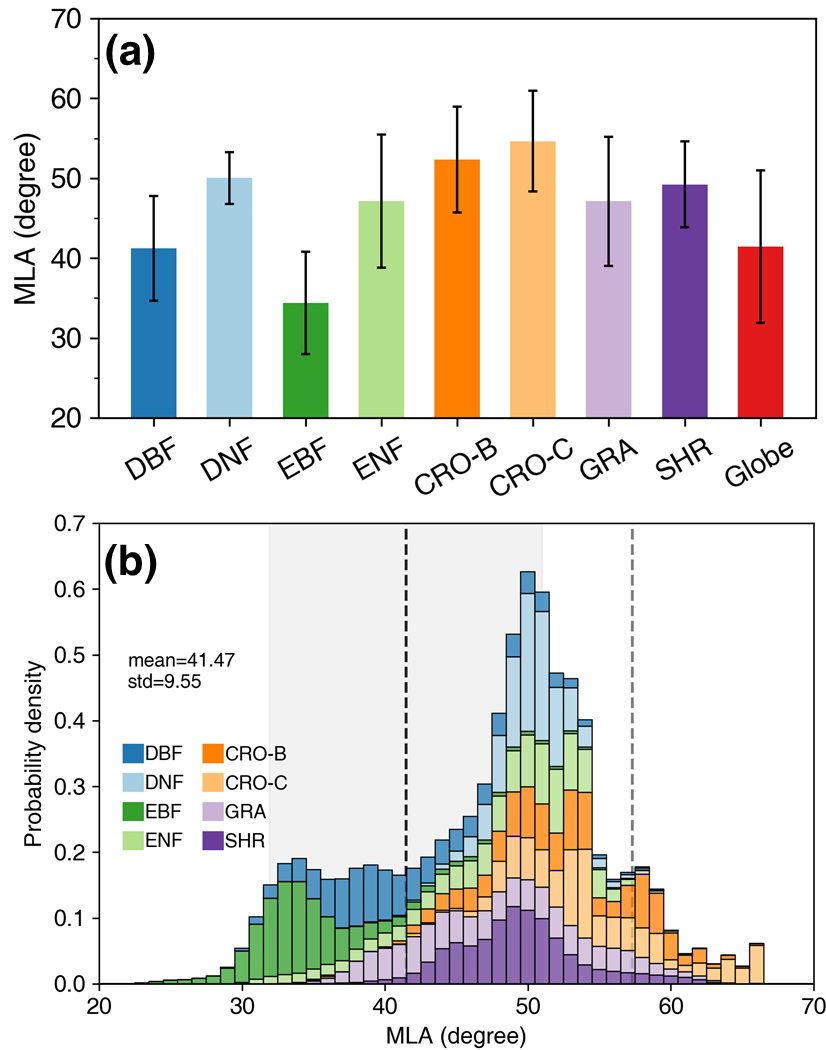


272
 273 **Figure 8.** The global mean leaf inclination angle (MLA) map. The right panel shows the MLA latitudinal mean (solid line) and the
 274 standard deviation values (shaded area) weighted by leaf area index.

275 **Table 4.** Statistics of global mean leaf inclination angle (MLA), nadir leaf projection function ($G(0)$), and inclination index (χ_L) for
 276 different plant functional types (PFT). STD is the standard deviation. The χ_L is converted from MLA ($\chi_L = 2\cos(\text{MLA}) - 1$) ([Lawrence](#)
 277 [et al., 2019](#)).

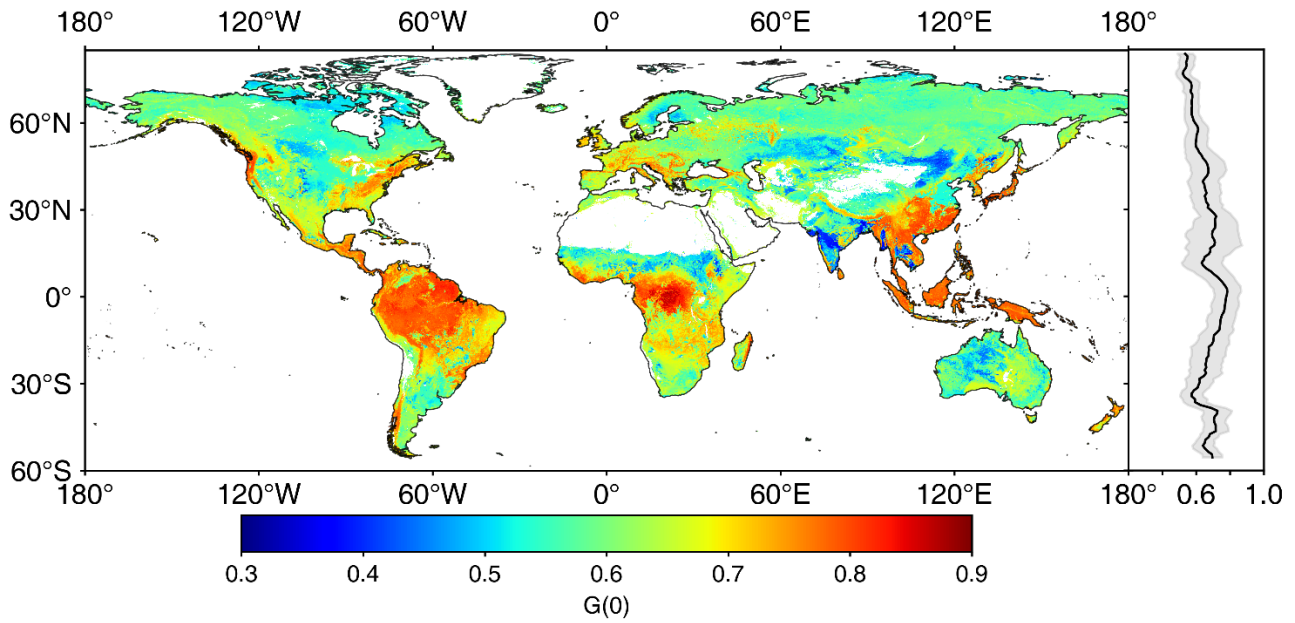
PFT	DBF	DNF	EBF	ENF	CRO-B	CRO-C	GRA	SHR	Globe
Area proportion(%)	14.02	6.32	15.08	11.42	2.99	6.84	28.45	14.88	100.00
MLA($^\circ$)	41.23	50.05	34.40	47.13	52.35	54.65	47.12	49.23	41.47
STD of MLA ($^\circ$)	6.58	3.24	6.42	8.35	6.63	6.28	8.08	5.35	9.55
$G(0)$	0.69	0.58	0.76	0.61	0.55	0.52	0.61	0.59	0.68
STD of $G(0)$	0.07	0.03	0.06	0.08	0.07	0.08	0.09	0.06	0.11
χ_L	0.50	0.28	0.65	0.36	0.22	0.16	0.36	0.31	0.50

278
 279 The global MLA exhibits an asymmetric probability density distribution toward the lower MLA (Fig. 9b). It roughly
 280 presents three peaks, with the highest peak ($\sim 51^\circ$) containing DNF, ENF, CRO, GRA, and SHR. The moderate peak ($\sim 35^\circ$)
 281 is mainly composed of EBF and DBF, while the third peak ($\sim 58^\circ$) is dominated by crops. The MLAs of crops and some
 282 grasslands are close to the MLA of the spherical distribution (57.30°). The global MLA (41.47°) is 15.83° (38%) smaller
 283 than the MLA of the spherical distribution because the vegetation MLA is mostly less than 57.30° (Fig. 9b).



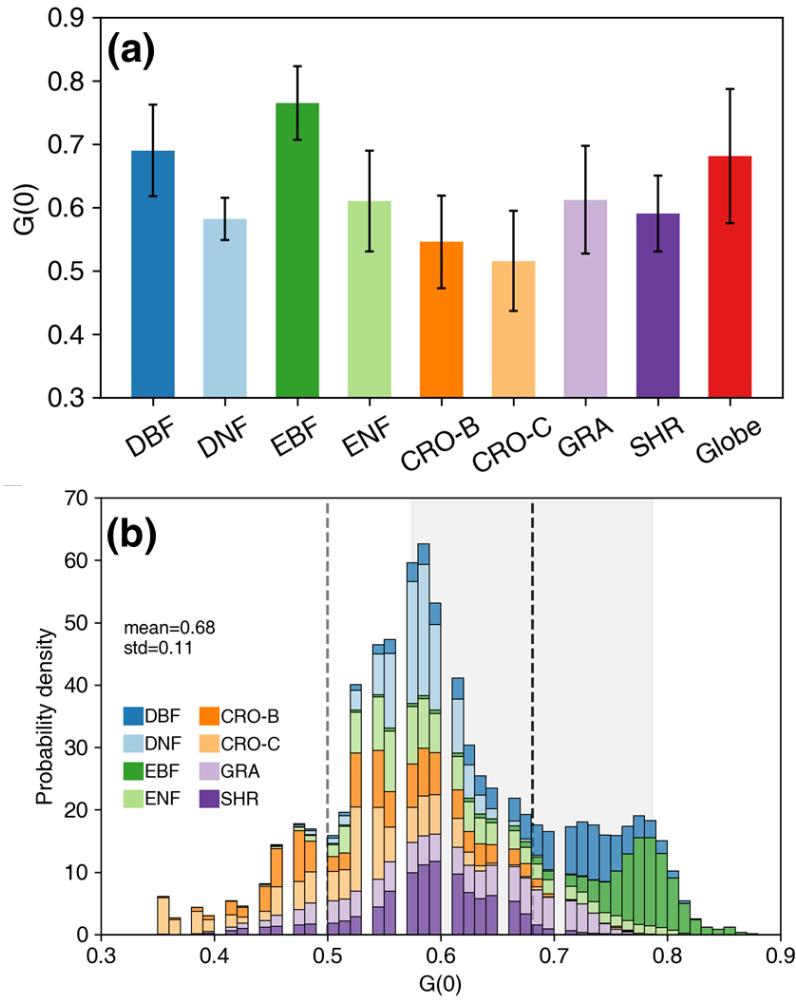
284
 285 **Figure 9.** Statistics (a) and probability density distributions (b) of the global mean leaf inclination angle (MLA) for different plant
 286 functional types. The error bars in (a) represent the standard deviation. The black dash line and shade area in (b) indicate the global MLA
 287 mean and standard deviation. The gray dashed line represents the MLA ($=57.30^\circ$) of spherical leaf angle distribution. The mean, standard
 288 deviation, and probability density values are weighted by leaf area index. See Fig. 1 for the acronyms.

289 Fig. 10 displays the spatial distribution of global $G(0)$ generated from MLA. Overall, the global $G(0)$ shows an opposite
 290 pattern with the global MLA. The $G(0)$ values in Central Asia (grasslands, Fig. S2), southern India (cereal crops), and the
 291 central United States (grasslands and cereal crops) are relatively lower than those in tropical rainforests, forests in Southeast
 292 Asia, and forests in the eastern United States. $G(0)$ generally decreases slowly with latitude, from 0.78 ± 0.08 at the equator
 293 ($\sim 1.5^\circ$ N) to 0.52 ± 0.04 in the northern tundra ($\sim 76.5^\circ$ N).



294
 295 **Figure 10.** The global nadir leaf projection function ($G(0)$) map. The right panel shows the $G(0)$ mean (solid line) and standard deviation
 296 values (shaded area) weighted by leaf area index.

297 Among different PFTs, EBF has the highest $G(0)$, at approximately 0.76 ± 0.06 (Fig. 11a, Table 4), whereas cereal crops
 298 show the lowest value, at approximately 0.52 ± 0.08 . The DBF $G(0)$ is comparable to the global average. The $G(0)$ of broad-
 299 leaved forests is greater than that of other PFTs (Fig. 11a, Table 4). The global $G(0)$ probability density distribution peaks at
 300 0.52–0.65, with an asymmetric distribution (Fig. 11b). The proportion on the right side of the peak is larger than that on the
 301 left. The peak of the global $G(0)$ distribution mainly contains DNF, ENF, CRO, GRA, and SHR. The left side of the peak is
 302 mainly composed of crops, while the right side is dominated by broad-leaved forests and some shrubs. The spherical
 303 distribution $G(0)$ (0.50) is mainly represented by crops and a small amount of grassland, where $G(0)$ also shows a large
 304 variation (~ 0.35). The spherical distribution $G(0)$ is 0.18 (26%) less than the global average $G(0)$ (0.68), as most vegetation
 305 $G(0)$ is greater than 0.50 (Fig. 11b).

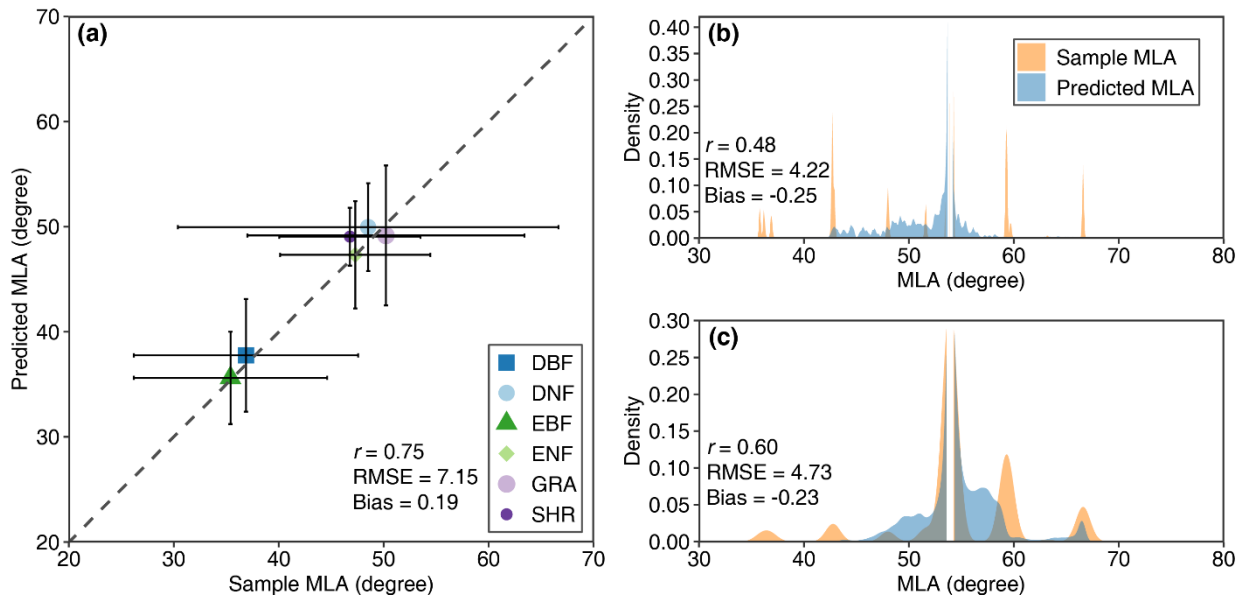


306

307 **Figure 11.** Statistics (a) and probability density distributions (b) of the global nadir leaf projection function ($G(0)$) for different plant
 308 functional types. The error bars in (a) represent the standard deviation. The black dash line and shade area in (b) indicate the global $G(0)$
 309 mean and standard deviation. The gray dashed line represents the $G(0)$ ($=0.50$) of spherical leaf angle distribution. The mean, standard
 310 deviation, and probability density values are weighted by leaf area index. See Fig. 1 for the acronyms.

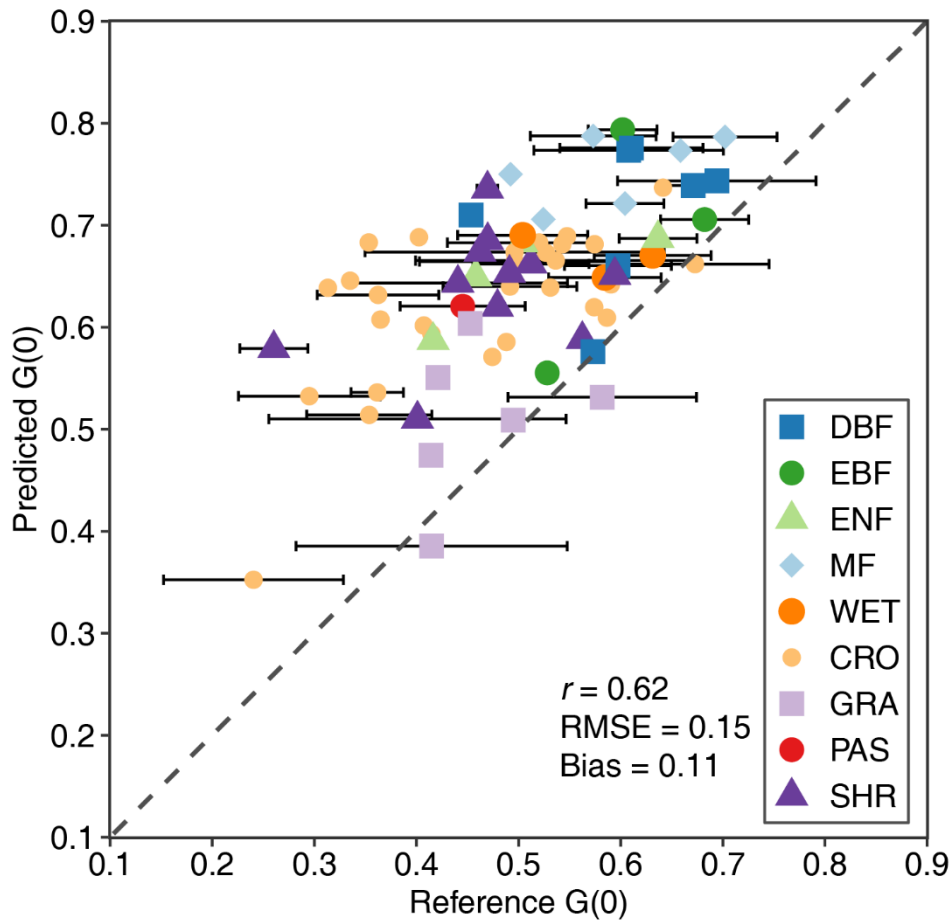
311 3.4 Evaluation of global MLA

312 Fig. 12 shows the comparison between the predicted MLA and upscaled MLA samples using the ten-fold cross-validation
 313 method. For noncrops, the predicted MLA is moderately consistent with the upscaled sample MLA ($r = 0.75$, $RMSE =$
 314 7.15°), with 83% of samples having residuals $< 10^\circ$ and 94% of samples having residuals $< 15^\circ$. For DNF and SHR, the
 315 predicted MLA compresses the variation range of sample MLA (Fig. 12a). For crops, the predicted MLA of CRO-C shows
 316 higher consistency ($r = 0.60$) than that of CRO-B ($r = 0.48$). (Fig. 12b and c).



317
 318 **Figure 12.** Comparisons between predicted MLA and sample MLA for noncrop (a), broadleaf crops (b), and cereal crops (c) (See Fig. 1
 319 for the acronyms). The error bar in (a) represents the standard deviation.

320 Fig. 13 compares $G(0)$ derived from the MLA and high-resolution reference data. The MLA-derived $G(0)$ shows moderate
 321 consistency with the reference $G(0)$ ($r = 0.62$), and 65% of the estimated $G(0)$ residuals are < 0.15 , and 84% of the residuals
 322 are < 0.20 . The estimated $G(0)$ generally overestimates ($bias = 0.11$), especially when $G(0)$ is low (< 0.60), mainly for crops,
 323 pasture, woody wetlands, and shrubs, whereas grasslands show better consistency. The estimated $G(0)$ is temporally more
 324 stable than the reference $G(0)$ which is generally greater than 0.50 and displays seasonal variation (horizontally distributed
 325 bars in Fig. 13).



326

327 **Figure 13.** Comparisons of $G(0)$ derived from mean leaf inclination angle and high-resolution reference data for different plant functional
 328 types (see Fig. 2 for the acronyms). The error bar represents the standard deviation of reference $G(0)$ at different seasons.

329 4 Discussion

330 4.1 Global MLA and $G(0)$

331 This study compiled global LIA field measurements and generated the first global 500 m MLA and $G(0)$ maps (Figs. 8 and
 332 10). These maps show the average MLA and $G(0)$ conditions during the growing seasons from 2001 to 2022. Overall, the
 333 global MLA is lowest around the equator and increases with latitude (Figs. 8 and 10). This accords with the MLA latitude
 334 variation derived from model simulations (Huemmrich, 2013). Crops have higher MLA than broadleaf forests whose leaves
 335 are relatively horizontal. The global MLA and $G(0)$ maps enhance our understanding of the global distribution of MLA and
 336 $G(0)$ and should be useful in radiative transfer modeling, remote sensing of vegetation parameters, land surface modeling,
 337 and ecological studies.

338 The globally derived MLA is 41.47° , which is consistent with the LIA measurements (40.74° , Tables 3 and 4). However, the
 339 derived MLAs of DBF, DNF, CRO-B, and SHR are approximately 10° greater than the measured MLAs. It is noted that the
 340 number and spatial distribution of LIA measurements for these biomes are limited. For example, the global CRO-B areas are
 341 dominated by soybeans with higher LIA (Table S2), and the LIA measurements for soybeans are limited, which caused the
 342 CRO-B MLA in the global map to be greater than that in the measurement statistics (Tables 3 and 4). The poor crop MLA
 343 prediction (Fig. 12b) is mainly caused by a small number of samples and the strong seasonal variation. It is difficult to
 344 consider within-crop LIA variation when typical MLA values are assigned to different crops.
 345 Due to the lack of high-resolution reference MLA, the global MLA was evaluated through a comparison of the MLA-derived
 346 $G(0)$ with the high-resolution reference $G(0)$ (Fig. 13). This practice was adopted because both MLA and $G(0)$ are closely
 347 related. $G(0)$ is typically calculated from the LIA distribution function based on Nilson's algorithm (Nilson, 1971). We
 348 calculated $G(0)$ from MLA assuming an ellipsoidal LIA distribution (De Wit, 1965) and found that the calculated $G(0)$ is
 349 highly consistent with the reference $G(0)$ calculated from the Nilson's algorithm for different theoretical LIA distributions
 350 (Fig. S5). The MLA-calculated $G(0)$ also shows a monotonic decreasing relationship with MLA (Fig. S6).
 351 The result shows medium consistency but MLA-derived $G(0)$ overestimates at low values (< 0.60), especially for CRO, PAS,
 352 SHR, and WET. The overestimation may be partly caused by the underestimation of MLA at high values that is related to
 353 the errors introduced in the sample expansion and upscaling. These errors are mainly caused by a lack of LIA measurements,
 354 vegetation structural complexity, and seasonal variation. In addition, the uncertainties in the reference $G(0)$ may have
 355 contributed to the overestimation. The reference $G(0)$ was derived from the Beer-Lambert law (Eq. (4)) which assumes that
 356 the canopy is a turbid medium. The turbid medium assumption is unrealistic for complex vegetation (Widlowski et al., 2014).
 357 The angular variation of CI and the mixture of branches and leaves in generating high-resolution $G(0)$ can also lead to the
 358 overestimation. Previous studies have shown that CI increases with the view zenith angle (Fang, 2021), which means that the
 359 whole $CI > CI(0)$ and can lead to the underestimation of the reference $G(0)$ (Eq. (6) and (7)). The mixture of branches and
 360 leaves may result in the underestimation of the reference $G(0)$ due to the usually higher inclination angle of the trunks (Liu et
 361 al., 2019). The MODIS LAI product used for LIA upscaling in the $G(0)$ validation (section 2.4) is known to have issues such
 362 as internal inconsistency, backup algorithm accuracy, and spatiotemporal gaps (Kandasamy et al., 2013; Pu et al., 2023;
 363 Zhang et al., 2024). In the future, new improved MODIS LAI can be used in the $G(0)$ validation (Pu et al., 2024; Yan et al.,
 364 2024). Compared with the previous $G(0)$ derived from global vegetation biophysical products (Eq. (7)) ($R^2 = 0.11$, $RMSE =$
 365 0.53) (Li et al., 2022), the MLA-derived $G(0)$ performs better ($R = 0.62$, $RMSE = 0.15$). In addition, the $G(0)$ data obtained
 366 from our study can be used to derive the $G(\theta)$ for any arbitrary angle. One method of getting $G(\theta)$ is based on single-
 367 parameter ellipsoidal leaf angle distribution (Campbell, 1990) (Eq. (3)). Another method is to make use of both $G(0)$ and
 368 $G(57.3^\circ)$ ($\equiv 0.5$) and derive $G(\theta)$ using a simple linear ($G(\theta) = a \cdot \theta + b$) or sinusoidal ($G(\theta) = a \cdot \sin(\theta) + b$)
 369 interpolation method. Since $G(\theta)$ varies most significantly in the nadir direction for different MLA (Wilson, 1959), the
 370 uncertainty of $G(\theta)$ derived from the global MLA in other directions will be smaller than that of $G(0)$.

372 **4.2 The relationship between MLA and other variables**

373 Analysis of the relationships between MLA and other features in the MLA mapping process reveals that MLA is negatively
374 correlated with NDVI, NIR reflectance, and NIR BRDF kernel coefficients (Fig. 7). These findings are consistent with other
375 simulation and experimental studies ([Zou and Möttus, 2015](#); [Liu et al., 2012](#); [Dong et al., 2019](#); [Jacquemoud et al., 1994](#)).
376 Higher LIA means lower radiation interception, more NIR downward radiation, and lower NIR reflectance ([Liu et al., 2012](#)).
377 This results in negative correlations between MLA and NIR reflectance and vegetation index. The negative relationships
378 between MLA and radiation, precipitation, and temperature (Fig. 7) are related to the vegetation adaptation mechanism.
379 Under suitable climate conditions (radiation, precipitation, and temperature), horizontal leaves are formed to absorb more
380 radiation and increase the photosynthesis rate ([Van Zanten et al., 2010](#); [King, 1997](#)). The positive correlation between MLA
381 and the standard deviation of radiation and temperature (Fig. 7) indicates that the MLA is more vertical in areas with
382 significant seasonal changes in radiation and temperature (mid to high-latitude areas) because vertical leaves maximize
383 intercepted radiation under low solar altitudes at mid to high-latitude areas ([Huemmrich, 2013](#)).
384 This study predicted global MLA with 40 variables (Fig. 6). To explore the regional differences of the variable importance,
385 an analysis was conducted for the tropical (23.5°S-23.5°N), northern temperate (23.5°N-60°N), northern polar (60°N-90°N),
386 and the southern temperate (23.5°S-60°S) zones. The 40 most important variables are similar among different regions
387 although minor differences exist (Fig. S7). Among the 40 variables for tropical, northern temperate, northern polar, and
388 southern temperate zones, 32, 35, 30, and 31 of them, respectively, are the same as the 40 global variables (Fig. S7). Climate
389 and spectral variables are significant among all regions, whereas BRDF features are the most important in the southern
390 temperate zone. The 40 most important variables in the global MLA prediction account for ~ 80% of total importance among
391 different regions, which is similar to that in the global prediction.

392 **4.3 Use of the new MLA map**

393 The spherical LAD assumption has been widely adopted in the literature ([Tang et al., 2016](#); [Zhao et al., 2020](#); [Wang and](#)
394 [Fang, 2020](#)). This study demonstrates that the spherical assumption is valid only for cereal crops, but not for broadleaf
395 forests (Tables 3 and 4). This finding is consistent with previous local LIA measurements ([De Wit, 1965](#); [Pisek et al., 2013](#);
396 [Yan et al., 2021](#)). For crops, the spherical assumption may even become invalid because of seasonality and species diversity
397 (Table S2, Figs. 5 and 9). Fig. 13 shows that most of the reference G(0) values are greater than 0.50, while the spherical
398 distribution would underestimate the interception of radiation and rainfall (Figs. 9 and 11) ([Stadt and Loeffers, 2000](#)). In
399 current LSMs, a constant LIA is commonly assigned for each PFT ([Majasalmi and Bright, 2019](#)). For example, the
400 Community Land Model V5 (CLM5) (Table S4) ([Lawrence et al., 2019](#)) uses lower inclination indices and higher LIA
401 values than our results (Tables 3 and 4) and thus may underestimate canopy interception. The global LIA map generated in
402 this study provides a more reasonable LIA parameterization strategy for the application communities.

403 4.4 Limitations and prospects

404 The limitations of this study mainly relate to the small number of LIA measurements, especially continuous measurements.
405 First, within-species LIA variations were neglected in the spatial expansion due to limited spatial coverage of existing LIA-
406 measured data (Section 2.3.1). This may introduce some errors, especially for crops. Second, three different sources of LIA
407 measurements were gathered with different sampling schemes and methods. The random forest algorithm is robust to these
408 differences because part of samples and features are randomly selected and the algorithm ensembles the predications from
409 multiple decision trees ([Svetnik et al., 2003](#)). Third, for forests, the contribution of the understory was not considered.
410 Typically, the understory is characterized by more horizontal leaves, and ignoring the understory may lead to an MLA
411 overestimation ([Utsugi et al., 2006](#)). Nevertheless, a previous study showed that the relative contribution of the understory to
412 the overall MLA is less than 10% ([Li et al., 2022](#)). Finally, only the growing season MLA was calculated, whereas the
413 seasonal and long-term variations of MLA were not considered due to the lack of continuous LIA measurements.
414 Eq. (1) assumed a linear relationship between LAI and EVI2 in the 500 m upscaling process. Global analysis of MODIS LAI
415 and EVI2 shows a non-linear relationship between the two variables (Fig. S8). This non-linear relationship was also used to
416 upscale MLA, and the derived MLA was found consistent with the original one (Fig. S9) because of the homogeneity of the
417 500 m pixel after rigorous sample screening (section 2.3.1).
418 In the future, more efficient LIA observation systems should be developed to provide continuous LIA data ([Kattenborn et al.,](#)
419 [2022](#)). LIA measurements can be integrated into existing ground observation networks, such as the National Ecological
420 Observatory Network (NEON) ([Kao et al., 2012](#)), Integrated Carbon Observation System (ICOS) ([Gielen et al., 2018](#)), and
421 Terrestrial Ecosystem Research Network (TERN) ([Karan et al., 2016](#)), to enhance temporal LIA measurements in larger
422 spatial extent, especially for DNF and crops. Using standard LIA measurement protocols will certainly improve the LIA data
423 consistency ([Li et al., 2023](#)). Multiangle reflectance ([Jacquemoud et al., 2009](#); [Goel and Thompson, 1984](#); [Jacquemoud et al.,](#)
424 [1994](#)) or light detection and ranging ([Zheng and Moskal, 2012](#); [Bailey and Mahaffee, 2017](#); [Itakura and Hosoi, 2019](#)) are
425 encouraging remote sensing tools that can help to derive temporally continuous and high-resolution MLA data.

426 5 Conclusion

427 This study compiled existing global LIA measurements and generated the first global 500 m MLA and G(0) products by
428 gap-filling the LIA measurement data using a random forest regressor. The mean of global LIA measurements is 40.74° and
429 cereal crops show the highest MLA (59.11°). The global MLA shows an explicit spatial distribution and the value increases
430 with latitude. The global MLA is $41.47^{\circ} \pm 9.55^{\circ}$ and follows the order of CRO-C > CRO-B > DNF > SHR > ENF \approx GRA >
431 DBF > EBF. The predicted MLA presents a medium consistency ($r = 0.75$, RMSE = 7.15°) with the validation samples for
432 noncrops. For crops, the results are relatively poorer ($r = 0.48$ and 0.60 for broadleaf crops and cereal crops) because of
433 limited LIA measurements and strong seasonality. The G(0) derived from MLA is moderately consistent with the reference
434 G(0) ($r = 0.62$).

435 The MLA and G(0) products obtained in this study would enhance our understanding of global LIA and assist remote
436 sensing retrieval and land surface modeling studies. These products provide a more realistic parameterization strategy than
437 the commonly used spherical LAD and PFT-specific MLA assignment. Note the global MLA and G(0) products mainly
438 represent the typical state during the growing season. These products can be further improved and temporal MLA data can
439 be obtained through continuous measurements and remote sensing retrieval.

440 **Data availability**

441 The global MLA and G(0) products are available in: Li, S. and Fang, H. 2024, <https://doi.org/10.5281/zenodo.10940673>. ([Li](#)
442 [and Fang, 2024](#)). The related code can be accessed at https://code.earthengine.google.com/?accept_repo=users/SiJia/MTA.

443 **Author contributions**

444 HF and SL conceptualized this work. SL compiled global LIA measurements, generated global products, and curated the
445 datasets. SL and HF wrote the manuscript. HF was responsible for funding and supervision.

446 **Competing interests**

447 The contact author has declared that none of the authors has any competing interests.

448 **Acknowledgements**

449 The authors are grateful to TRY and many other researchers for sharing the LIA measurement data. Jens Kattge at the Max
450 Planck Institute for Biogeochemistry and Dongliang Cheng at Fujian Normal University provided the TRY species location
451 data and LIA measurements in China's subtropical regions, respectively.

452

453 **Financial support**

454 This work was mainly supported by the National Natural Science Foundation of China (42171358).

455 **References**

456 Alexandridis, T. K., Ovakoglou, G., and Clevers, J. G. P. W.: Relationship between MODIS EVI and LAI across time and
457 space, Geocarto International, 35, 1385-1399, 10.1080/10106049.2019.1573928, 2019.

458 Bailey, B. N. and Mahaffee, W. F.: Rapid measurement of the three-dimensional distribution of leaf orientation and the leaf
 459 angle probability density function using terrestrial LiDAR scanning, *Remote Sens. Environ.*, 194, 63-76,
 460 10.1016/j.rse.2017.03.011, 2017.

461 Bayat, B., van der Tol, C., and Verhoef, W.: Integrating satellite optical and thermal infrared observations for improving
 462 daily ecosystem functioning estimations during a drought episode, *Remote Sens. Environ.*, 209, 375-394,
 463 10.1016/j.rse.2018.02.027, 2018.

464 Boryan, C., Yang, Z., Mueller, R., and Craig, M.: Monitoring US agriculture: the US department of agriculture, national
 465 agricultural statistics service, cropland data layer program, Geocarto International, 26, 341-358, 2011.

466 Brown, L. A., Meier, C., Morris, H., Pastor-Guzman, J., Bai, G., Lerebourg, C., Gobron, N., Lanconelli, C., Clerici, M., and
 467 Dash, J.: Evaluation of global leaf area index and fraction of absorbed photosynthetically active radiation products over
 468 North America using Copernicus Ground Based Observations for Validation data, *Remote Sens. Environ.*, 247,
 469 10.1016/j.rse.2020.111935, 2020.

470 Campbell, G.: Derivation of an angle density function for canopies with ellipsoidal leaf angle distributions, *Agricultural and*
 471 *forest meteorology*, 49, 173-176, 1990.

472 Chen, J. M., Ju, W., Ciais, P., Viovy, N., Liu, R., Liu, Y., and Lu, X.: Vegetation structural change since 1981 significantly
 473 enhanced the terrestrial carbon sink, *Nat Commun*, 10, 4259, 10.1038/s41467-019-12257-8, 2019.

474 Chen, X., Zhong, Q.-L., Lyu, M., Wang, M., Hu, D., Sun, J., and Cheng, D.: Trade-off relationship between light
 475 interception and leaf water shedding at different canopy positions of 73 broad-leaved trees of Yangji Mountain in Jiangxi
 476 Province, China, *SCIENTIA SINICA Vitae*, 51, 91-101, 10.1360/SSV-2020-0218, 2021.

477 Chianucci, F., Pisek, J., Raabe, K., Marchino, L., Ferrara, C., and Corona, P.: A dataset of leaf inclination angles for
 478 temperate and boreal broadleaf woody species, *Annals of Forest Science*, 75, 50-50, 10.1007/s13595-018-0730-x, 2018.

479 Crawford, C. J., Roy, D. P., Arab, S., Barnes, C., Vermote, E., Hulley, G., Gerace, A., Choate, M., Engebretson, C.,
 480 Micijevic, E., Schmidt, G., Anderson, C., Anderson, M., Bouchard, M., Cook, B., Dittmeier, R., Howard, D., Jenkerson, C.,
 481 Kim, M., Kleyians, T., Maersperger, T., Mueller, C., Neigh, C., Owen, L., Page, B., Pahlevan, N., Rengarajan, R., Roger, J.-
 482 C., Sayler, K., Scaramuzza, P., Skakun, S., Yan, L., Zhang, H. K., Zhu, Z., and Zahn, S.: The 50-year Landsat collection 2
 483 archive, *Science of Remote Sensing*, 8, 100103, <https://doi.org/10.1016/j.srs.2023.100103>, 2023.

484 d'Andrimont, R., Verhegghen, A., Lemoine, G., Kempeneers, P., Meroni, M., and van der Velde, M.: From parcel to
 485 continental scale – A first European crop type map based on Sentinel-1 and LUCAS Copernicus in-situ observations,
 486 *Remote Sens. Environ.*, 266, 112708, <https://doi.org/10.1016/j.rse.2021.112708>, 2021.

487 de Wit, C. T.: *Photosynthesis of leaf canopies*, Pudoc, 1965.

488 Dong, J., fu, y., wang, j., Tian, H., Fu, S., Niu, Z., Han, W., Zheng, Y., Huang, J., and Yuan, W.: 30m winter wheat
 489 distribution map of China for four years (2016-2019), 10.6084/m9.figshare.12003990.v2, 2020.

490 Dong, T., Liu, J., Shang, J., Qian, B., Ma, B., Kovacs, J. M., Walters, D., Jiao, X., Geng, X., and Shi, Y.: Assessment of red-
 491 edge vegetation indices for crop leaf area index estimation, *Remote Sens. Environ.*, 222, 133-143, 10.1016/j.rse.2018.12.032,
 492 2019.

493 Fang, H.: Canopy clumping index (CI): A review of methods, characteristics, and applications, *Agricultural and Forest*
 494 *Meteorology*, 303, 108374, <https://doi.org/10.1016/j.agrformet.2021.108374>, 2021.

495 Fang, H., Li, S., Zhang, Y., Wei, S., and Wang, Y.: New insights of global vegetation structural properties through an
 496 analysis of canopy clumping index, fractional vegetation cover, and leaf area index, *Science of Remote Sensing*, 100027,
 497 <https://doi.org/10.1016/j.srs.2021.100027>, 2021.

498 Fisette, T., Rollin, P., Aly, Z., Campbell, L., Daneshfar, B., Filyer, P., Smith, A., Davidson, A., Shang, J., and Jarvis, I.:
 499 AAFC annual crop inventory, 2013 Second International Conference on Agro-Geoinformatics (Agro-Geoinformatics), 270-
 500 274,

501 Foley, J. A., Prentice, I. C., Ramankutty, N., Levis, S., Pollard, D., Sitch, S., and Haxeltine, A.: An integrated biosphere
 502 model of land surface processes, terrestrial carbon balance, and vegetation dynamics, *Global biogeochemical cycles*, 10,
 503 603-628, 1996.

504 Gielen, B., Acosta, M., Altimir, N., Buchmann, N., Cescatti, A., Ceschia, E., Fleck, S., Hörtnagl, L., Klumpp, K., Kolari, P.,
 505 Lohila, A., Loustau, D., Mara  n-Jimenez, S., Manise, T., Matteucci, G., Merbold, L., Metzger, C., Moureaux, C.,
 506 Montagnani, L., Nilsson, M. B., Osborne, B., Papale, D., Pavelka, M., Saunders, M., Simioni, G., Soudani, K., Sonnentag,
 507 O., Tallec, T., Tuittila, E.-S., Peichl, M., Pokorny, R., Vincke, C., and Wohlfahrt, G.: Ancillary vegetation measurements at
 508 ICOS ecosystem stations, *International Agrophysics*, 32, 645-664, 10.1515/intag-2017-0048, 2018.

509 Goel, N. S. and Thompson, R. L.: Inversion of vegetation canopy reflectance models for estimating agronomic variables. V.
 510 Estimation of leaf area index and average leaf angle using measured canopy reflectances, *Remote Sens. Environ.*, 16, 69-85,
 511 10.1016/0034-4257(84)90028-2, 1984.

512 Han, J., Zhang, Z., Luo, Y., Cao, J., Zhang, L., Cheng, F., Zhuang, H., Zhang, J., and Tao, F.: NESEA-Rice10: high-
 513 resolution annual paddy rice maps for Northeast and Southeast Asia from 2017 to 2019, *Earth System Science Data*, 13,
 514 5969-5986, 10.5194/essd-13-5969-2021, 2021.

515 Hinojo-Hinojo, C. and Goulden, M.: A compilation of canopy leaf inclination angle measurements across plant species and
 516 biome types, 10.7280/D1T97H, 2020.

517 Huemmrich, K. F.: Simulations of Seasonal and Latitudinal Variations in Leaf Inclination Angle Distribution: Implications
 518 for Remote Sensing, *Advances in Remote Sensing*, 02, 93-101, 10.4236/ars.2013.22013, 2013.

519 Itakura, K. and Hosoi, F.: Estimation of Leaf Inclination Angle in Three-Dimensional Plant Images Obtained from Lidar,
 520 *Remote Sensing*, 11, 10.3390/rs11030344, 2019.

521 Jacquemoud, S., Flasse, S., Verdebout, J., and Schmuck, G.: Comparison of Several Optimization Methods To Extract
 522 Canopy Biophysical Parameters - Application To Caesar Data, 291-298, 1994.

523 Jacquemoud, S., Verhoef, W., Baret, F., Bacour, C., Zarco-Tejada, P. J., Asner, G. P., François, C., and Ustin, S. L.:
 524 PROSPECT+SAIL models: A review of use for vegetation characterization, *Remote Sens. Environ.*, 113, S56-S66,
 525 10.1016/j.rse.2008.01.026, 2009.

526 Kandasamy, S., Baret, F., Verger, A., Neveux, P., and Weiss, M.: A comparison of methods for smoothing and gap filling
 527 time series of remote sensing observations—application to MODIS LAI products, *Biogeosciences*, 10, 4055-4071, 2013.

528 Kao, R. H., Gibson, C. M., Gallery, R. E., Meier, C. L., Barnett, D. T., Docherty, K. M., Blevins, K. K., Travers, P. D.,
 529 Azuaje, E., Springer, Y. P., Thibault, K. M., McKenzie, V. J., Keller, M., Alves, L. F., Hinckley, E.-L. S., Parnell, J., and
 530 Schimel, D.: NEON terrestrial field observations: designing continental-scale, standardized sampling, *Ecosphere*, 3, art115,
 531 10.1890/es12-00196.1, 2012.

532 Karan, M., Liddell, M., Prober, S. M., Arndt, S., Beringer, J., Boer, M., Cleverly, J., Eamus, D., Grace, P., Van Gorsel, E.,
 533 Hero, J. M., Hutley, L., Macfarlane, C., Metcalfe, D., Meyer, W., Pendall, E., Sebastian, A., and Wardlaw, T.: The
 534 Australian SuperSite Network: A continental, long-term terrestrial ecosystem observatory, *Sci. Total Environ.*, 568, 1263-
 535 1274, 10.1016/j.scitotenv.2016.05.170, 2016.

536 Kattenborn, T., Richter, R., Guimarães-Steinicke, C., Feilhauer, H., and Wirth, C.: AngleCam: Predicting the temporal
 537 variation of leaf angle distributions from image series with deep learning, *Methods in Ecology and Evolution*, 13, 2531-2545,
 538 10.1111/2041-210x.13968, 2022.

539 Kattge, J., Bonisch, G., Diaz, S., Lavorel, S., and Prentice, I. C.: TRY plant trait database - enhanced coverage and open
 540 access, *Glob Chang Biol*, 26, 119-188, 10.1111/gcb.14904, 2020.

541 King, D. A.: The Functional Significance of Leaf Angle in Eucalyptus, *Aust. J. Bot.*, 45, 619-639,
 542 <https://doi.org/10.1071/BT96063>, 1997.

543 Kuusk, A.: A two-layer canopy reflectance model, *Journal of Quantitative Spectroscopy and Radiative Transfer*, 71, 1-9,
 544 [https://doi.org/10.1016/S0022-4073\(01\)00007-3](https://doi.org/10.1016/S0022-4073(01)00007-3), 2001.

545 Lang, A. R. G.: Leaf orientation of a cotton plant, *Agricultural Meteorology*, 11, 37-51, 10.1016/0002-1571(73)90049-6,
 546 1973.

547 Lawrence, D. M., Fisher, R. A., Koven, C. D., Oleson, K. W., Swenson, S. C., Bonan, G., Collier, N., Ghimire, B., Van
 548 Kampenhout, L., and Kennedy, D.: The Community Land Model version 5: Description of new features, benchmarking, and
 549 impact of forcing uncertainty, *Journal of Advances in Modeling Earth Systems*, 11, 4245-4287, 2019.

550 Li, S. and Fang, H.: Global Leaf Inclination Angle (LIA) and Nadir Leaf Projection Function (G(0)) Products, Zenodo
 551 [dataset], 10.5281/zenodo.10940673, 2024.

552 Li, S., Fang, H., and Zhang, Y.: Determination of the Leaf Inclination Angle (LIA) through Field and Remote Sensing
 553 Methods: Current Status and Future Prospects, *Remote Sensing*, 15, 946, 2023.

554 Li, S., Fang, H., Zhang, Y., and Wang, Y.: Comprehensive evaluation of global CI, FVC, and LAI products and their
 555 relationships using high-resolution reference data, *Science of Remote Sensing*, 6, 10.1016/j.srs.2022.100066, 2022.

556 Liu, J., Pattey, E., and Jégo, G.: Assessment of vegetation indices for regional crop green LAI estimation from Landsat
 557 images over multiple growing seasons, *Remote Sens. Environ.*, 123, 347-358, 10.1016/j.rse.2012.04.002, 2012.

558 Liu, J., Wang, T., Skidmore, A. K., Jones, S., Heurich, M., Beudert, B., and Premier, J.: Comparison of terrestrial LiDAR
 559 and digital hemispherical photography for estimating leaf angle distribution in European broadleaf beech forests, *ISPRS*
 560 *Journal of Photogrammetry and Remote Sensing*, 158, 76-89, 10.1016/j.isprsjprs.2019.09.015, 2019.

561 Maes, W. and Steppe, K.: Estimating evapotranspiration and drought stress with ground-based thermal remote sensing in
 562 agriculture: a review, *J. Exp. Bot.*, 63, 4671-4712, 2012.

563 Majasalmi, T. and Bright, R. M.: Evaluation of leaf-level optical properties employed in land surface models – example with
 564 CLM 5.0, *Geoscientific Model Development Discussions*, 1-24, 2019.

565 Mantilla-Perez, M. B. and Salas Fernandez, M. G.: Differential manipulation of leaf angle throughout the canopy: current
 566 status and prospects, *J. Exp. Bot.*, 68, 5699-5717, 2017.

567 Muñoz-Sabater, J., Dutra, E., Agustí-Panareda, A., Albergel, C., Arduini, G., Balsamo, G., Boussetta, S., Choulga, M.,
 568 Harrigan, S., Hersbach, H., Martens, B., Miralles, D. G., Piles, M., Rodríguez-Fernández, N. J., Zsoter, E., Buontempo, C.,
 569 and Thépaut, J.-N.: ERA5-Land: a state-of-the-art global reanalysis dataset for land applications, *Earth System Science Data*,
 570 13, 4349-4383, 10.5194/essd-13-4349-2021, 2021.

571 Myneni, R., Knyazikhin, Y., Park, T.: MCD15A2H MODIS/Terra+Aqua Leaf Area Index/FPAR 8-day L4 Global 500m SIN
 572 Grid V006 [dataset], <http://doi.org/10.5067/MODIS/MCD15A2H.006>, 2015.

573 Nilson, T.: A theoretical analysis of the frequency of gaps in plant stands, *Agricultural Meteorology*, 8, 25-38, 1971.

574 Norman, J. M. and Campbell, G. S.: Canopy structure, in: *Plant Physiological Ecology: Field methods and instrumentation*,
 575 edited by: Pearcy, R. W., Ehleringer, J. R., Mooney, H. A., and Rundel, P. W., Springer Netherlands, Dordrecht, 301-325,
 576 10.1007/978-94-009-2221-1_14, 1989.

577 Pisek, J. and Adamson, K.: Dataset of leaf inclination angles for 71 different Eucalyptus species, *Data Brief*, 33, 106391,
 578 10.1016/j.dib.2020.106391, 2020.

579 Pisek, J., Ryu, Y., and Alikas, K.: Estimating leaf inclination and G-function from leveled digital camera photography in
 580 broadleaf canopies, *Trees*, 25, 919-924, 10.1007/s00468-011-0566-6, 2011.

581 Pisek, J., Sonnentag, O., Richardson, A. D., and Möttus, M.: Is the spherical leaf inclination angle distribution a valid
 582 assumption for temperate and boreal broadleaf tree species?, *Agricultural and Forest Meteorology*, 169, 186-194,
 583 10.1016/j.agrformet.2012.10.011, 2013.

584 Pisek, J., Diaz-Pines, E., Matteucci, G., Noe, S., and Rebmann, C.: On the leaf inclination angle distribution as a plant trait
 585 for the most abundant broadleaf tree species in Europe, *Agricultural and Forest Meteorology*, 323,
 586 10.1016/j.agrformet.2022.109030, 2022.

587 Pu, J., Yan, K., Roy, S., Zhu, Z., Rautiainen, M., Knyazikhin, Y., and Myneni, R. B.: Sensor-independent LAI/FPAR CDR:
 588 reconstructing a global sensor-independent climate data record of MODIS and VIIRS LAI/FPAR from 2000 to 2022, *Earth*
 589 *System Science Data*, 16, 15-34, 10.5194/essd-16-15-2024, 2024.

590 Pu, J., Yan, K., Gao, S., Zhang, Y., Park, T., Sun, X., Weiss, M., Knyazikhin, Y., and Myneni, R. B.: Improving the MODIS
 591 LAI compositing using prior time-series information, *Remote Sens. Environ.*, 287, 10.1016/j.rse.2023.113493, 2023.

592 Raabe, K., Pisek, J., Sonnentag, O., and Annuk, K.: Variations of leaf inclination angle distribution with height over the
 593 growing season and light exposure for eight broadleaf tree species, *Agricultural and Forest Meteorology*, 214-215, 2-11,
 594 10.1016/j.agrformet.2015.07.008, 2015.

595 Ross, J.: Radiative transfer in plant communities, *Vegetation and the Atmosphere*, 13-55, 1975.

596 Ross, J.: The radiation regime and architecture of plant stands, 3, Springer Science & Business Media 1981.

597 Ryu, Y., Sonnentag, O., Nilson, T., Vargas, R., Kobayashi, H., Wenk, R., and Baldocchi, D. D.: How to quantify tree leaf
 598 area index in an open savanna ecosystem: A multi-instrument and multi-model approach, *Agricultural and Forest*
 599 *Meteorology*, 150, 63-76, 10.1016/j.agrformet.2009.08.007, 2010.

600 Schaaf, C. and Wang, Z.: MCD43A4 MODIS/Terra+Aqua BRDF/Albedo Nadir BRDF Adjusted Ref Daily L3 Global -
 601 500m V006, NASA EOSDIS Land Processes Distributed Active Archive Center [dataset],
 602 <https://doi.org/10.5067/MODIS/MCD43A4.006>, 2015a.

603 Schaaf, C. and Wang, Z.: MCD43A1 MODIS/Terra+Aqua BRDF/Albedo Model Parameters Daily L3 Global - 500m V006,
 604 NASA EOSDIS Land Processes Distributed Active Archive Center [dataset],
 605 <https://doi.org/10.5067/MODIS/MCD43A1.006>, 2015b.

606 Sellers, P. J.: Canopy reflectance, photosynthesis and transpiration, *International Journal of Remote Sensing*, 6, 1335-1372,
 607 10.1080/01431168508948283, 1985.

608 Shen, R., Dong, J., Yuan, W., Han, W., Ye, T., and Zhao, W.: A 30-m Resolution Distribution Map of Maize for China
 609 Based on Landsat and Sentinel Images, *Journal of Remote Sensing*, 2022, doi:10.34133/2022/9846712, 2022.

610 Stadt, K. J. and Lieffers, V. J.: MIXLIGHT: a flexible light transmission model for mixed-species forest stands, *Agricultural*
 611 *and Forest Meteorology*, 102, 235-252, 2000.

612 Sulla-Menashe, D., Gray, J. M., Abercrombie, S. P., and Friedl, M. A.: Hierarchical mapping of annual global land cover
 613 2001 to present: The MODIS Collection 6 Land Cover product, *Remote Sens. Environ.*, 222, 183-194,
 614 10.1016/j.rse.2018.12.013, 2019.

615 Svetnik, V., Liaw, A., Tong, C., Culberson, J. C., Sheridan, R. P., and Feuston, B. P.: Random forest: a classification and
 616 regression tool for compound classification and QSAR modeling, *Journal of chemical information and computer sciences*, 43,
 617 1947-1958, 2003.

618 Tadono, T., Ishida, H., Oda, F., Naito, S., Minakawa, K., and Iwamoto, H.: Precise global DEM generation by ALOS
 619 PRISM, *ISPRS Annals of the Photogrammetry, Remote Sensing and Spatial Information Sciences*, 2, 71-76, 2014.

620 Tang, H., Ganguly, S., Zhang, G., Hofton, M. A., Nelson, R. F., and Dubayah, R.: Characterizing leaf area index (LAI) and
 621 vertical foliage profile (VFP) over the United States, *Biogeosciences*, 13, 239-252, 10.5194/bg-13-239-2016, 2016.

622 Toda, M., Ishihara, M. I., Doi, K., and Hara, T.: Determination of species-specific leaf angle distribution and plant area
623 index in a cool-temperate mixed forest from UAV and upward-pointing digital photography, *Agricultural and Forest*
624 *Meteorology*, 325, 10.1016/j.agrformet.2022.109151, 2022.

625 Utsugi, H., Araki, M., Kawasaki, T., and Ishizuka, M.: Vertical distributions of leaf area and inclination angle, and their
626 relationship in a 46-year-old *Chamaecyparis obtusa* stand, *For. Ecol. Manage.*, 225, 104-112,
627 <https://doi.org/10.1016/j.foreco.2005.12.028>, 2006.

628 van Zanten, M., Pons, T. L., Janssen, J. A. M., Voisenek, L. A. C. J., and Peeters, A. J. M.: On the Relevance and Control of
629 Leaf Angle, *Crit. Rev. Plant Sci.*, 29, 300-316, 10.1080/07352689.2010.502086, 2010.

630 Verhoef, W., Jia, L., Xiao, Q., and Su, Z.: Unified Optical-Thermal Four-Stream Radiative Transfer Theory for
631 Homogeneous Vegetation Canopies, *IEEE Transactions on Geoscience and Remote Sensing*, 45, 1808-1822,
632 10.1109/TGRS.2007.895844, 2007.

633 Wang, W. M., Li, Z. L., and Su, H. B.: Comparison of leaf angle distribution functions: Effects on extinction coefficient and
634 fraction of sunlit foliage, *Agricultural and Forest Meteorology*, 143, 106-122, 10.1016/j.agrformet.2006.12.003, 2007.

635 Wang, Y. and Fang, H.: Estimation of LAI with the LiDAR Technology: A Review, *Remote Sensing*, 12,
636 10.3390/rs12203457, 2020.

637 Weiss, M. and Baret, F.: CAN-EYE V6.4.91 User Manual, [https://www6.paca.inrae.fr/can-](https://www6.paca.inrae.fr/can-eye/Documentation/Documentation)
638 [eye/Documentation/Documentation](https://www6.paca.inrae.fr/can-eye/Documentation/Documentation), 2017.

639 Widlowski, J.-L., Côté, J.-F., and Béland, M.: Abstract tree crowns in 3D radiative transfer models: Impact on simulated
640 open-canopy reflectances, *Remote Sens. Environ.*, 142, 155-175, 10.1016/j.rse.2013.11.016, 2014.

641 Wilson, J.: Inclined point quadrats, *New Phytol.*, 59, 1-7, 10.1111/j.1469-8137.1960.tb06195.x, 1960.

642 Wilson, J. W.: Analysis of the spatial distribution of foliage by two-dimensional point quadrats, *New Phytol.*, 58, 92-99,
643 <https://doi.org/10.1111/j.1469-8137.1959.tb05340.x>, 1959.

644 Xiao, Q., McPherson, E. G., Ustin, S. L., and Grismer, M. E.: A new approach to modeling tree rainfall interception, *Journal*
645 *of Geophysical Research: Atmospheres*, 105, 29173-29188, 2000.

646 Yan, G., Jiang, H., Luo, J., Mu, X., Li, F., Qi, J., Hu, R., Xie, D., and Zhou, G.: Quantitative Evaluation of Leaf Inclination
647 Angle Distribution on Leaf Area Index Retrieval of Coniferous Canopies, *Journal of Remote Sensing*, 2021, 1-15,
648 10.34133/2021/2708904, 2021.

649 Yan, K., Wang, J., Peng, R., Yang, K., Chen, X., Yin, G., Dong, J., Weiss, M., Pu, J., and Myneni, R. B.: HiQ-LAI: a high-
650 quality reprocessed MODIS leaf area index dataset with better spatiotemporal consistency from 2000 to 2022, *Earth System*
651 *Science Data*, 16, 1601-1622, 10.5194/essd-16-1601-2024, 2024.

652 You, N., Dong, J., Huang, J., Du, G., Zhang, G., He, Y., Yang, T., Di, Y., and Xiao, X.: The 10-m crop type maps in
653 Northeast China during 2017-2019, *Sci Data*, 8, 41, 10.1038/s41597-021-00827-9, 2021.

654 Zhang, X., Yan, K., Liu, J., Yang, K., Pu, J., Yan, G., Heiskanen, J., Zhu, P., Knyazikhin, Y., and Myneni, R. B.: An Insight
655 Into the Internal Consistency of MODIS Global Leaf Area Index Products, *IEEE Transactions on Geoscience and Remote*
656 *Sensing*, 62, 1-16, 10.1109/tgrs.2024.3434366, 2024.

657 Zhao, J., Li, J., Liu, Q., Xu, B., Yu, W., Lin, S., and Hu, Z.: Estimating fractional vegetation cover from leaf area index and
658 clumping index based on the gap probability theory, *International Journal of Applied Earth Observation and Geoinformation*,
659 90, 102-112, 10.1016/j.jag.2020.102112, 2020.

660 Zheng, G. and Moskal, L. M.: Leaf orientation retrieval from terrestrial laser scanning (TLS) data, *IEEE Transactions on*
661 *Geoscience and Remote Sensing*, 50, 3970-3979, 10.1109/TGRS.2012.2188533, 2012.

662 Zou, X. and Möttus, M.: Retrieving crop leaf tilt angle from imaging spectroscopy data, *Agricultural and Forest Meteorology*,
663 205, 73-82, 10.1016/j.agrformet.2015.02.016, 2015.

664 Zou, X., Möttus, M., Tammeorg, P., Torres, C. L., Takala, T., Pisek, J., Mäkelä, P., Stoddard, F. L., and Pellikka, P.:
665 Photographic measurement of leaf angles in field crops, *Agricultural and Forest Meteorology*, 184, 137-146,
666 10.1016/j.agrformet.2013.09.010, 2014.

667

668